CONCRETE FRACTURE MECHANICS AND SIZE EFFECT USING A SPECIALIZED COHESIVE ZONE MODEL

BY

KYOUNGSOO PARK

B.E., Hanyang University, 2003

THESIS

Submitted in partial fulfillment of the requirements
for the degree of Master of Science in Civil and Environmental Engineering
in the Graduate College of the
University of Illinois at Urbana-Champaign, 2005

Urbana, Illinois

Abstract

The size effect is the change of structural properties, especially nominal strength, due to scaling of geometrically similar structures. Due to the relatively large non-linear fracture process zone, the size effect on the nominal strength of a concrete structure is explained by non-linear fracture mechanics employing both an equivalent elastic crack model and a cohesive zone model (CZM) approach. The concept of equivalent elastic crack model provides the theoretical background for the size effect method (SEM) and the two-parameter fracture model (TPFM), which provide two size-independent fracture parameters. In addition, the CZM characterizes non-linear fracture process behavior through the bi-linear softening curve, which is determined by four experimental fracture parameters: tensile strength ($f_t{}'$), initial fracture energy (G_f), total fracture energy (G_F) and critical crack tip opening displacement ($CTOD_c$). The location of the kink point in the bi-linear softening model has been estimated empirically in the literature. Thus a formal criterion to determine the kink point is proposed and discussed. The bi-linear softening curve in the CZM enables prediction of the load versus crack mouth opening displacement (CMOD) experimental curves as well as the size effect. Several examples and a sensitivity analysis are given to illustrate these points.

To my parents

Acknowledgments

It is my great pleasure to thank those researchers and friends for assisting me in this endeavor. I would like to express my profound gratitude to my advisor Professor Glaucio H. Paulino. Without his enthusiasm, knowledge and support, it would have been impossible for me to complete this work. I am also indebted to Professor Jeffery R. Roesler for his invaluable suggestions and encouragement.

I would like to thank my colleague, M. Cristian Gaedicke, for the experiments on concrete material and for our discussions of concrete fracture behavior. In addition, I am beholden to my group members, Matthew C. Walters, Alok Sutradhar, Zhengyu Zhang, Seong-Hyeok Song, Huiming Yin, Bin Shen, Eshan V. Dave, Mariana Silva, Shun Wang, Chau H. Le and Maribel Gonzalez. I will always remember their valuable suggestions and warm encouragement. I would also like to thank my friends who accompany and believe in each other, although we are separated by great distance. I am especially grateful to Ann Spear for reviewing my thesis.

I can not express enough appreciation to my parents and wonderful sister. Their perpetual support and trust, for whatever I do, wherever I am, are always with me.

This thesis was supported from a study conducted in the Center of Excellence for Airport Technology, funded by the Federal Aviation Administration under Research Grant Number 95-C-001 and the University of Illinois.

Table of Contents

List of Tables

List of Figures

Chapter 1

Introduction

Concrete structures experience the formation of large cracking zones before reaching the tensile strength of the material. In general, due to the relatively large process zone, the strength of concrete depends on the structural size considered. This relationship is called the size effect [7]. In this chapter, background is provided with respect to: size effect, mechanisms of crack growth in concrete, and a few numerical models. Then, the organization of thesis is briefly outlined.

1.1 Background

A fundamental issue for the evaluation of concrete structures is to interpret experimental values, like maximum load of a specimen, as values that are applicable to a structure in the field. For instance, the strength of a concrete beam in the laboratory is different from the strength of a concrete beam for an actual structure due to the difference of the beam sizes. This is because the strength of a concrete structure depends not only on the tensile strength of concrete, but also on the size of the structure, called the size effect. In this study, fracture mechanics is employed to demonstrate the size effect of concrete.

1.1.1 Size Effect

In general, the size effect due to scaling of geometrically similar structures can be characterized by the nominal strength of the structure, the maximum deflection and the maximum strain. This study focuses on the nominal strength (σ_{Nu}) of concrete, which is conventionally proportional to the maximum load divided by a representative cross sectional area. As a result, the size effect can be represented as the deviation from the nominal strength for geometrically similar structures. The influence of structure size on the nominal strength is explained by the boundary layer effect, the statistical size effect and the fracture mechanics size effect [6, 7, 8].

Boundary layer effect

Concrete behaves differently on the boundary of a structure than in the interior. This is called the boundary layer effect, and results from the different ratio of aggregates in different regions of concrete structures. There is relatively less aggregate on the surface boundary of concrete structures than in the interior. Therefore, the material property varies between the surface boundary and the interior. If the size of the boundary layer is assumed to be independent of structural size, a small specimen would exhibit more influence of the boundary layer effect than a large specimen. Another boundary layer effect is described by the Poisson's ratio effect. This effect reflects the plane stress condition on the surface boundary and the plane strain condition in the interior. This size effect can be reduced by using geometrically similar structures with the same thickness [6].

Statistical size effect

The study of the size effect on strength originated from the statistical aspects of material randomness. In the 1500's, Leonardo da Vinci claimed that "Among cords of equal thickness, the longest is the least strong [36]." Later, Griffith [19] illustrated experimentally that the smaller the diameter of a glass fiber, the higher its nominal strength because a smaller

structure has less probability to contain defects that result in the material failure. Finally, the principles of the statistical size effect were established by the pioneering work of Weibull [35]. However, for quasi-brittle materials like concrete, the statistical size effect is dominated by the fracture mechanics size effect [6].

Fracture mechanics size effect

Fracture mechanics provides an explanation for the relationship between size and material strength. The power scaling law of linear elastic fracture mechanics (LEFM) illustrates the size effect based on the failure criterion without the consideration of the length scale dimension (characteristic length). On the other hand, the energetic approach of non-linear fracture mechanics, containing the characteristic length scale dimension, demonstrates the size effect law for quasi-brittle materials [8].

1.1.2 Mechanisms of Crack Growth in Concrete

In general, a concrete structure undergoes distributed microcracks, the bridging zone and a traction free microcrack [2, 34], as shown in Figure 1.1(a). Microcracks initiate ahead of the bridging zone before the stress reaches tensile strength ($f_t{}'$). When the stress reaches the tensile strength ($f_t{}'$), microcracks grow and coalesce, which generates the bridging zone, also called the non-linear process zone (Figure 1.1(b)). This zone, which transfers stress between cracked surfaces, results from the crack overlapping and branching, and from the weak interface between aggregates and cement paste (matrix). The non-linear process zone bridges the microcrack zone and a traction free macrocrack. When a crack opening width is greater than a certain value, called the final crack opening width (w_f), a macroscopic crack appears, which cannot transfer traction along cracked surfaces anymore.

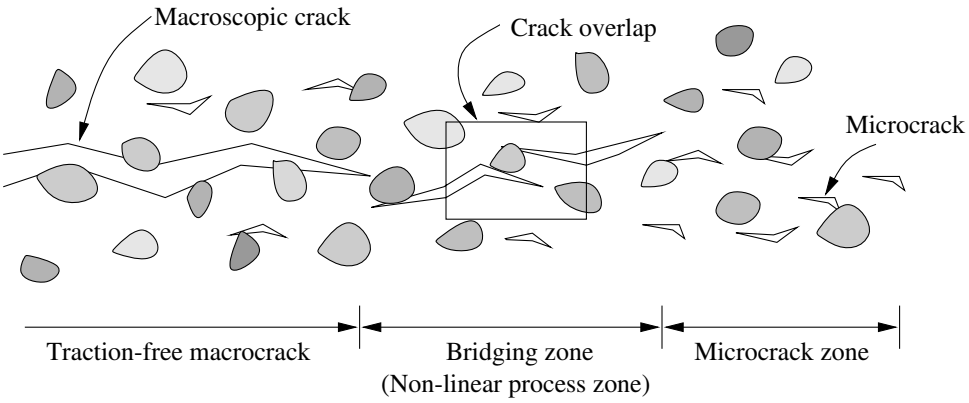

(a)

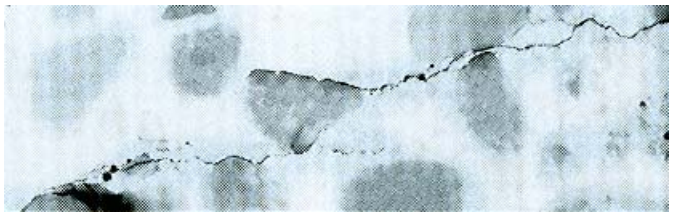

(b)

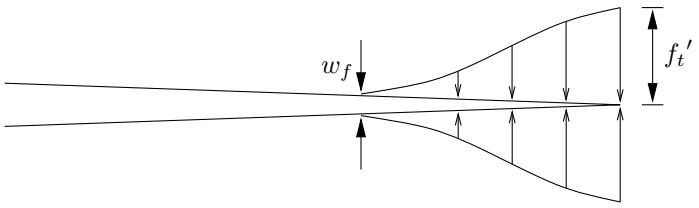

(c)

Figure 1.1: (a) Mechanisms of mode I crack growth in concrete [2]; (b) crack interface bridging [34]; and (c) idealized process zone by the cohesive zone model [21].

1.1.3 Numerical Models

Numerical models of fracture can be classified by the observation scales of fracture, which varies from the atomistic level (Figure 1.2(a)) to the micro level (Figure 1.2(b)), to the macro level (Figure 1.2(c)). For the modeling of macroscopic cracks, the finite element method (FEM) is usually exploited on the basis of continuum mechanics. Discontinuity of fracture is embedded at the macroscopic continuum level by introducing local quantities like a damaged zone. For instance, insertion of cohesive surface elements can characterize the

non-linear process zone and a traction-free macrocrack at the macro level, called the cohesive zone model, as shown in Figure 1.1(c). Moreover, a fracture description at the micro level is complicated, because of the discrete nature of material failure, such as fracture and fragmentation. In order to simulate this discontinuity, the discrete element method (DEM) is developed so that a solid is replaced with a discontinuous particle composite [15]. In contrast to continuum models, the discontinuous composite results in stress and displacement discontinuity in space. Finally, on the atomistic level, molecular dynamic simulation is available by identifying interaction forces between particles with respect to atomistic coordinates [29].

A multi-scaling numerical model is proposed by Gao and Klein [18, 27], called the virtual internal bond (VIB) model. The VIB model is based on the Cauchy-Born rule which connects atomistic behavior in micro length scale with continuum behavior in macro length scale.

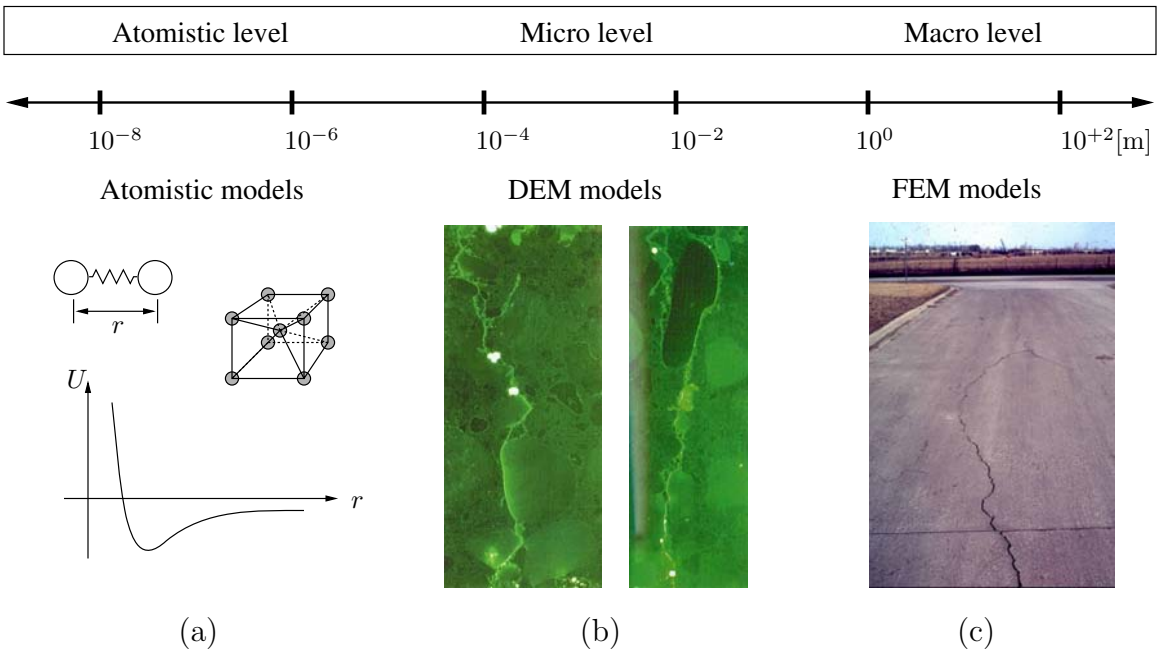

Figure 1.2: General observation scales of concrete fracture in numerical models. (a) schematic of atomistic model in which r is the distance and U is the atomistic potential; (b) crack face bridging and branching in high strength concrete and normal concrete [34]; and (c) longitudinal cracks in engineering scale concrete pavement.

1.2 Thesis Organization

This thesis contains five additional chapters : the size effect of concrete fracture, the cohesive zone model, the determination of the kink point in the bi-linear softening, the numerical predictions of the size effect in experiments, and the conclusions and future studies, respectively. First, the size effect of quasi-brittle materials, especially concrete, is discussed on the basis of fracture mechanics in Chapter 2. The concept of the equivalent elastic crack model, the size effect method, proposed by Bazant [4], and the two-parameter fracture model, proposed by Jenq and Shah [26], are demonstrated and compared. Next, the cohesive zone model, another approach to explain non-linear fracture mechanics, is discussed in Chapter 3. Essentially, the basic concept of the cohesive zone model, the determination of the bi-linear softening, and the implementation of the finite element analysis are described. Chapter 4 focuses on the determination of the kink point in a bi-linear softening curve, which is an essential feature of the cohesive zone model. The location of the kink point is hypothesized based on experimental fracture parameters provided by an integrated experimental validation and numerical verification. In Chapter 5, numerical results of the cohesive zone model are compared to experimental results from three-point bending tests. The bi-linear softening cohesive zone model is compared to the measured load versus crack mouth opening displacement curves for several geometrically similar specimens, and the size effect of the nominal strength are illustrated. Finally, this thesis ends with concluding remarks and suggestions for future studies.

Chapter 2

Size Effect of Concrete Fracture

A characteristic of concrete structures is size dependence of nominal strength, called the size effect. The size effect results from the relatively large non-linear fracture process zone, which has been interpreted by the concept of the equivalent elastic crack model [6]. In this chapter, linear and non-linear fracture mechanics are briefly reviewed. Next, fracture process behavior is explained. Then, the size effect is discussed based on fracture mechanics principles. Finally, the size effect method (SEM) [4] and the two-parameter fracture model (TPFM) [26] are discussed and compared based on the concept of the equivalent elastic crack model.

2.1 Review of Fracture Mechanics

2.1.1 Linear Elastic Fracture Mechanics

Linear elastic fracture mechanics (LEFM) was motivated by the work of Inglis [23] solving the elliptical hole problem for linear elastic material. However, a sharp crack results in stress singularity at the crack tip while the finite stress distribution around the crack tip exists in reality. Due to this discrepancy, Griffith [19] proposed the energy balance concept: a crack will propagate when the energy available to extend the unit area of crack is equal to the energy required. Later, this equivalent energy was called the energy release rate (G_I). In

1959, the stress intensity factor (K_I), introduced by Irwin [24], enabled calculation of the stress and the displacement at the asymptotic crack tip field. He also derived the relationship between G_I and K_I based on the crack closure analysis:

$$G_I = {K_I}^2/E \ , \tag{2.1}$$

where E is the Young's modulus of a material. The non-linear zone was assumed to be very small at the crack tip for the Griffith and Irwin approach to linear elastic material fracture.

2.1.2 Non-linear Fracture Mechanics

The LEFM is limited in its ability to analyze a material which has a large non-linear zone in front of a crack tip due to plastic yielding or to progressive softening. Rice [30] proposed the application of the path independent J-integral to a crack problem and proved that J is equal to the energy release rate for non-linear materials.

In 1961, Irwin [25] translated the non-linear fracture problem into LEFM through a plastic zone correction, later called the equivalent elastic crack model. By assuming a constant stress redistribution ahead of a crack tip and satisfying the global equilibrium, the plastic zone size (r_p) is calculated as follows

$$r_p = \frac{1}{\pi}\left(\frac{K_I}{f_t{}'}\right)^2 \ . \tag{2.2}$$

However, while the assumed constant stress distribution ahead of a crack tip is reasonable for a ductile metal, this is not valid for a quasi-brittle material like concrete, because of its progressive non-linear softening. The non-linear stress distribution ahead of a crack tip generates a larger fracture process zone, which is generally assumed to be proportional to the characteristic length (ℓ_{ch}) introduced by Hillerborg et al. [21],

$$\ell_{ch} = \left(\frac{K_I}{f_t{}'}\right)^2 = \frac{E' G_f}{{f_t{}'}^2} \tag{2.3}$$

where $E' = E$ for plane stress, $E' = E/(1-\nu^2)$ for plane strain, and G_f is the fracture energy. Through reasonable estimation of the fracture process zone size, we can obtain the effective crack length (a_{ec}) and the effective stress intensity factor in order to linearize the non-linear fracture problem.

In addition, to characterize brittleness of structural responses, the brittleness has been quantified so that a number provides small quantity for ductile behavior and large for elastic-brittle behavior [6]. For metals, the brittleness number (β_K) based on the plastic zone size (2.2) is

$$\beta_K = \frac{D f_t'^2}{K_I c^2} \ , \tag{2.4}$$

which provides the ASTM E 399 condition for validity of the fracture toughness test ($\beta_K \geq 2.5$). Similarly, brittleness numbers for concrete structural responses were proposed by Carpinteri [12], Hillerborg [22] and Bazant [4]. According to the characteristic length (2.3), for instance, the brittleness number increases when the strength of concrete increases and the fracture energy decreases.

Also, Barenblatt [3] and Dugdale [16] proposed the strip yield model, which approximates elastic-plastic behavior by superimposing crack closure stress on stress from a LEFM solution. This is the foundation of the cohesive zone model. Later, Hillerborg [21] expanded the CZM concept to concrete by combining fracture mechanics and the finite element method. The CZM will be discussed in the Chapter 3.

2.2 Fracture Process Behavior

In general, we classify fracture process behavior based on the size of the non-linear zone [6]. In front of a crack tip, the *fracture process zone*, or the non-linear softening zone, characterizes the progressive softening behavior (the gray area in Figure 2.1). The outer region of this zone (the black area in Figure 2.1) is named the *nonlinear hardening zone* which represents the hardening plasticity or perfect plasticity. For the first behavior type (Figure 2.1 (a)),

both the fracture process zone and the nonlinear hardening zone are relatively small such that the LEFM is applicable. Brittle materials such as glass, brittle ceramics and brittle metal, illustrate this type of fracture process behavior.

For the next type of behavior (Figure 2.1 (b)), because of the large nonlinear hardening zone and the small fracture process zone due to the plastic yielding, the elasto-plastic fracture mechanics can be exploited to analyze the the nonlinear hardening zone. Ductile materials (e.g. ductile metals) fall into the second behavior type.

The third type behavior (Figure 2.1 (c)) is strongly related to our study, which illustrates the progressive damage with material softening along the fracture process zone. While the nonlinear hardening zone might be negligible for this type, the relatively large fracture process zone significantly influences the stress redistribution. This behavior, called quasi-brittle, is found in concrete, rock, ice, paper, stiff clay, etc. The LEFM cannot be directly applied to these brittle materials because of the large nonlinear fracture process zone, which results in the size effect.

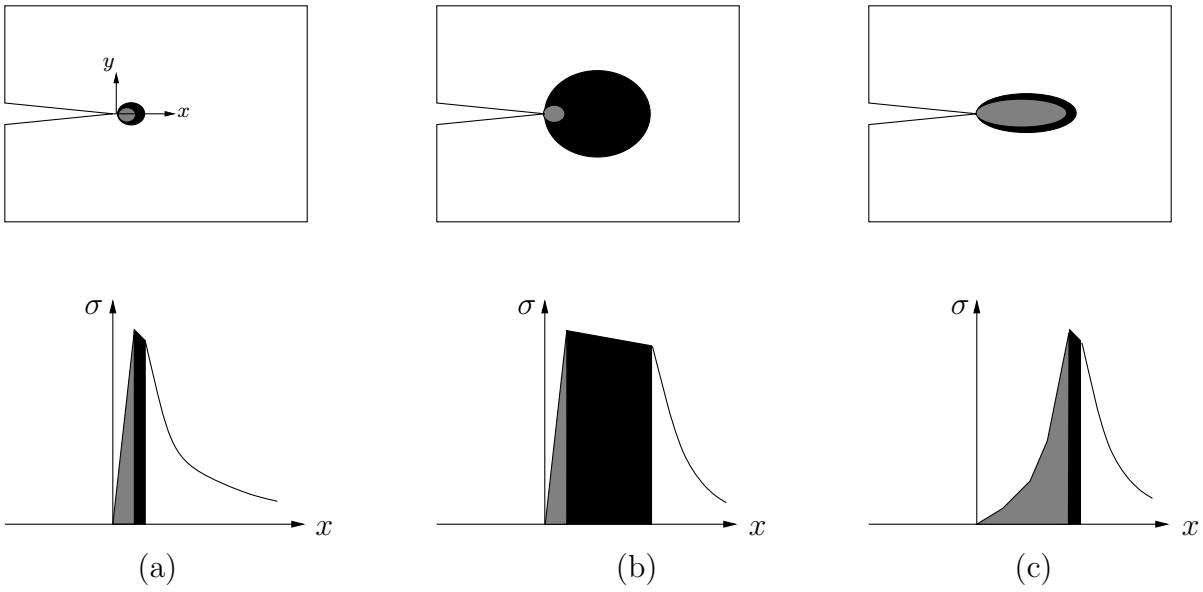

Figure 2.1: Types of fracture process behavior [6]

2.3 Fracture Mechanics Size Effect

2.3.1 Power Scaling Law

The power scaling law, as shown in Figure 2.2 [5], represents not only that nominal strength is independent of structure size based on the strength limit but also that the strength is proportional to $size^{-1/2}$ from the LEFM. First of all, we will derive the power scaling law by considering the three geometrically similar structures (D_0, $\bar{D}$, $\widetilde{D}$) with the corresponding responses (Y_0, $\bar{Y}$, $\widetilde{Y}$). Then, applying the "no-failure criterion" to the LEFM as well as to the classical strength theory, we will demonstrate strength that is independent of size and strength that is dependent on size.

To derive the power scaling law, let's consider a scaling law function which defines the relationship between structure size and corresponding response. A corresponding response is only dependent on the structure size ratio, $\mu = \bar{D}/D_0$, but independent of the choice of the reference size (D_0). The corresponding responses could be displacement, stress, strain or maximum load. A structure size (D_0) with a corresponding response (Y_0) is scaled to a structure size ($\bar{D} = \mu D_0$) with a corresponding response ($\bar{Y}$). Let the scaling law be $f(\mu)$, that is

$$\frac{\bar{Y}}{Y_0} = f(\mu) \ . \tag{2.5}$$

Consider another structure size ($\widetilde{D} = \lambda D_0$) with a corresponding response ($\widetilde{Y}$), i.e.

$$\frac{\widetilde{Y}}{Y_0} = f(\lambda) \ . \tag{2.6}$$

Because the corresponding response is independent of the reference size, by choosing the reference structure size $\widetilde{D}$ for the structure size $\bar{D}$, (2.5) and (2.6) generate

$$\frac{\bar{Y}}{\widetilde{Y}} = f\left(\frac{\mu}{\lambda}\right) = \frac{f(\mu)}{f(\lambda)} \ . \tag{2.7}$$

The derivative of (2.7) with respect to the μ leads to

$$\frac{1}{\lambda} f'\left(\frac{\mu}{\lambda}\right) = \frac{f'(\mu)}{f(\lambda)} \ . \tag{2.8}$$

When setting $\mu = \lambda$, we obtain the differential equation,

$$\frac{1}{\mu} f'(1) = \frac{f'(\mu)}{f(\mu)} \ . \tag{2.9}$$

Solution of this differential equation by the separation of variables produces

$$\ln f(\mu) = C + f'(1) \ln(\mu) \ . \tag{2.10}$$

The boundary condition is $f(\mu = 1) = 1$ obtained conceptually; if two structural sizes are the same, the corresponding responses are also identical, resulting in $C = 0$. Finally, we obtain the power scaling law function,

$$f(\mu) = \mu^{\alpha} \ , \tag{2.11}$$

which can be applicable to continuum mechanics if no characteristic dimension exists in the physical structure.

In order to evaluate the size effect on stress, we consider a structure size (D) with the corresponding responses: displacements ($\mathbf{u}$), stresses ($\boldsymbol{\sigma}$) and strains ($\boldsymbol{\epsilon}$). The structure size, D, is scaled to a structure size ($\bar{D} = \mu D$) with the corresponding responses ($\bar{\mathbf{u}}$, $\bar{\boldsymbol{\sigma}}$ and $\bar{\boldsymbol{\epsilon}}$). According to the power scaling law function (2.11), displacements of a scaled structure size ($\bar{\mathbf{u}}$) is assumed to be

$$\bar{\mathbf{u}} = \mu^{\alpha} \mathbf{u} \ . \tag{2.12}$$

Next, because stresses and strains are related to the first derivative of displacements, the

power laws of the stress and strain are

$$\bar{\boldsymbol{\sigma}} = \mu^{\alpha-1}\boldsymbol{\sigma} \quad \text{and} \quad \bar{\boldsymbol{\epsilon}} = \mu^{\alpha-1}\boldsymbol{\epsilon} \tag{2.13}$$

in continuum mechanics. In the end, we are able to apply the power scaling law to the failure criterion of both the strength limit and the LEFM.

For the plasticity or elasticity with the strength limit, the condition of "no-failure" with a structure size D, has the general form,

$$\phi(\boldsymbol{\sigma}, \boldsymbol{\epsilon}) < \sigma_0 \ . \tag{2.14}$$

For the scaled structure whose size is $\bar{D}$ and whose corresponding responses are $\bar{\boldsymbol{\sigma}}$ and $\bar{\boldsymbol{\epsilon}}$, the condition of no-failure should be identical although the structure sizes are different. As a result, in order to satisfy the "no-failure criterion",

$$\phi(\bar{\boldsymbol{\sigma}}, \bar{\boldsymbol{\epsilon}}) < \sigma_0 \ , \tag{2.15}$$

the power law constant of both the stress and the strain have to be zero ($\alpha - 1 = 0$) irregardless of the linear or non-linear function, ϕ. Thus, the stress is independent of the structure size (D), which is illustrated by the horizontal line in the Figure 2.2. Briefly, there is no size effect within the elastic or plastic strength limit.

The power law constant (α) based on the LEFM is different from that based on the strength theory because the "no-failure condition" is determined by the fracture toughness, which is generally equivalent to the J-integral [5, 8]. Then, the "no-failure condition" with a structure of size D is given by

$$J = \int_\Gamma \left(\frac{1}{2}\sigma_{ij}\epsilon_{ij}dx_2 - \sigma_{ij}n_j\frac{\partial u_i}{\partial x_1}ds \right) < G_I \ . \tag{2.16}$$

Similarly, a structure of size, D, is scaled to the structure size, $\bar{D}$, with corresponding responses ($\bar{\mathbf{u}}$ $\bar{\boldsymbol{\sigma}}$, $\bar{\boldsymbol{\epsilon}}$). To apply the scaling law, the substitution of (2.12) and (2.13) into (2.16) leads to

$$\begin{aligned}
\bar{J} &= \int_{\Gamma} \left(\frac{1}{2} (\mu^{\alpha-1}\sigma_{ij})(\mu^{\alpha-1}\epsilon_{ij}) \mu dx_2 - (\mu^{\alpha-1}\sigma_{ij}) n_j \frac{\partial \mu^{\alpha} u_i}{\partial \mu x_1} \mu ds \right) \\
&= \mu^{2\alpha-1} \int_{\Gamma} \left(\frac{1}{2} \sigma_{ij}\epsilon_{ij} dx_2 - \sigma_{ij} n_j \frac{\partial u_i}{\partial x_1} ds \right) \\
&= \mu^{2\alpha-1} J < G_I \ . \qquad (2.17)
\end{aligned}$$

Because the "no-failure condition" should be identical whether the structure is scaled or not, the exponent in (2.17) should be equal to zero, i.e. $2\alpha - 1 = 0$. Therefore, the nominal strength depends on the structure size (D), i.e. $\sigma_N \propto 1/\sqrt{D}$. If we plot this relation on the bi-logarithmic axis (Figure 2.2), the LEFM failure condition is represented by a straight line of slope $-1/2$. In conclusion, while the "no-failure criterion" for the strength limit (e.g. yield stress) illustrates no size effect, of LEFM (e.g. fracture energy) represents the size effect [5, 8].

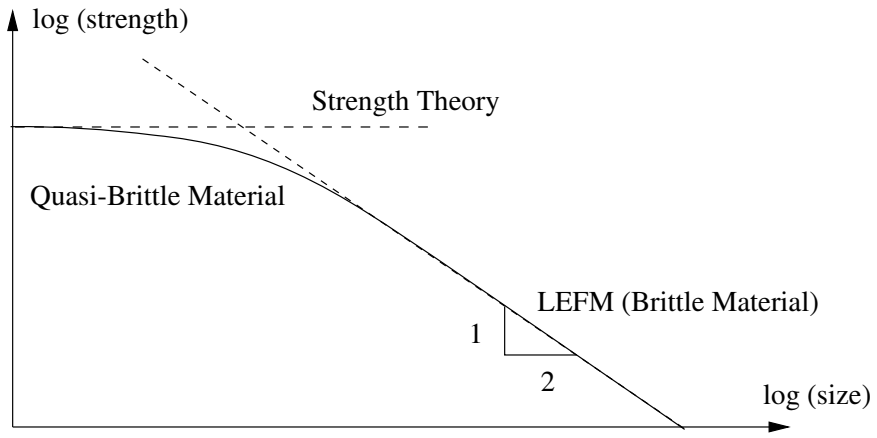

Figure 2.2: Size effect on the structure strength versus structure size in bi-logarithmic plot

2.3.2 Size Effect of Quasi-brittle Materials

For quasi-brittle materials, we can expect a smooth transition between the strength theory and the LEFM in Figure 2.2 because of the relatively large fracture process zone. The size effect of quasi-brittle materials connects two "no-failure criteria", the yield strength (f_t') for the strength theory and the fracture energy (G_f) for the LEFM. Consideration of both criteria provides the length dimension, which is generally considered to be a material property. Therefore, similarly to Irwin's plasticity zone size (2.2), a characteristic length dimension exists for quasi-brittle materials.

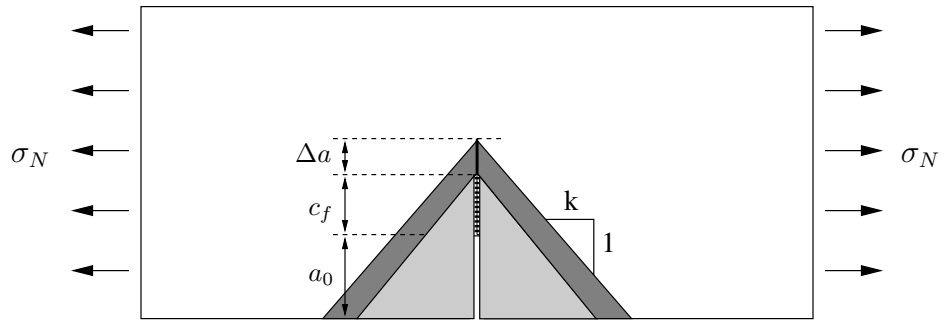

Figure 2.3: Energetic size effect law

The size effect can be demonstrated by the energy concept which states that the energy required to create a crack is the same as the energy available. While the required energy is the energy release rate times the fracture area, the available energy can be calculated by the decrease of the strain energy.

We consider a uniformly stressed (σ_N) plate having an initial notch (a_0) and a fracture process zone (c_f) as shown in Figure 2.3. Due to the far field stress, a crack propagates by length Δa under constant boundary displacement. During crack propagation, we assume that while the far field stress remains constant, the strain energy density changes from σ_N^2/E to zero only in the stress relief zone, the dark gray strip in Figure 2.3. As a result, the released strain energy is equal to $\sigma_N^2/2E$ times the stress relief zone. Equating the required and the

available energy leads to

$$G_f = 2k(a_0 + c_f) \times \frac{\sigma_N^2}{2E} \ . \tag{2.18}$$

Solving for the nominal stress, we obtain the size effect expression,

$$\sigma_N = \frac{Bf_t{}'}{\sqrt{1 + D/D_0}} \ , \tag{2.19}$$

where

$$Bf_t{}' = \sqrt{\frac{EG_f}{kc_f}} \quad \text{and} \quad D_0 = c_f \frac{D}{a_0} \ . \tag{2.20}$$

As a result, the size effect expression (2.19) shows that the nominal strength, σ_N, depends on the structure size, D, with respect to a characteristic length dimension, D_0, which is generally considered to be a material property. Furthermore, the brittleness number $\beta = D/D_0$ is introduced to make β independent of structural size and geometry [4]. In general, β is between 0.1 and 10 for quasi-brittle materials.

2.4 Equivalent Elastic Crack Model

The concept of the equivalent elastic crack model is exploited to implement the size effect method (SEM) by Bazant [6] and to implement the two-parameter fracture model (TPFM) by Jenq and Shah [33]. Both the SEM and the TPFM represent the size effect on the nominal strength depending on the structure size. In this section, the theoretical background of the two methods is discussed, and then the relationship between the SEM and the TPFM is given.

2.4.1 Size Effect Method

The theoretical background of the SEM is the equivalent elastic crack model applied to an idealized infinite structure size. Because the equivalent elastic crack increment Δa_{ec}

linearizes the non-linear fracture problems as shown in Figure 2.4, the nominal strength can be expressed by a stress intensity factor, K_{Ic}, a structure size, D, and a geometric function, $k(\alpha_{ec})$, based on the concept of the LEFM. Therefore, the nominal strength at the equivalent elastic crack tip can be expressed,

$$\sigma_{Nu} = \frac{K_{Ic}}{\sqrt{Dk^2(\alpha_{ec})}} \ . \tag{2.21}$$

Moreover, an increment of the equivalent crack length, Δa_{ec}, converges to the critical effective crack extension, c_f, which is generally assumed to be a material property. This is similar to Irwin's plastic zone size, as the structure dimensions approaches infinity.

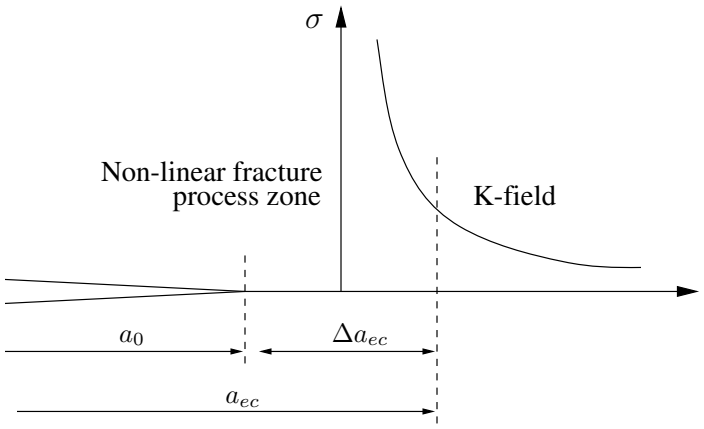

Figure 2.4: Equivalent elastic crack model

In order to derive the size effect implied in (2.21) considering an infinite structure size, which provides the relation, $\alpha_{ec} = \alpha_0 + c_f/D$, we obtain

$$\sigma_{Nu} = \frac{K_{Ic}}{\sqrt{Dk^2(\alpha_0 + c_f/D)}} \ . \tag{2.22}$$

Taking the Taylor series expansion of the geometric function, we obtain

$$k^2(\alpha_0 + c_f/D) = k^2(\alpha_0) + 2k(\alpha_0)k'(\alpha_0)\frac{c_f}{D} + \cdots \tag{2.23}$$

so that we eliminate the unknown material constant, c_f, in the geometric function. Because of the infinite structure size, we could take out the higher order terms in (2.23). Substituting (2.23) into (2.22) without higher order terms, we obtain the size effect expression,

$$\sigma_{Nu} = \frac{K_{Ic}}{\sqrt{k_0^2 D + 2k_0 k_0{}' c_f}} = \frac{B f_t{}'}{\sqrt{1 + D/D_0}} \ , \tag{2.24}$$

which is the same expression of the size effect law by the energy concept in the previous section given by (2.19) where

$$B f_t{}' = \frac{K_{Ic}}{\sqrt{2k_0 k_0{}' c_f}} \quad \text{and} \quad D_0 = \frac{2k_0{}'}{k_0} c_f \ . \tag{2.25}$$

The non-dimensional constant, B, and the length dimensional constant, D_0, can be determined by the experimental testing which provides the two fracture parameters, G_f and c_f, and by a linear regression plot [6].

2.4.2 Two-Parameter Fracture Model

The theoretical foundation of the TPFM is the equivalent elastic crack model. The experimental loading-unloading procedure enables the separation of the elastic response ($CMOD_{ec}$) and the plastic response ($CMOD_{pc}$), and provides both the loading compliance (C_i) and the unloading compliance (C_u) as illustrated in Figure 2.5. These experimental values result in the determination of the two fracture parameters in the TPFM: the stress intensity factor (K_{Ic}) and the critical crack tip opening width ($CTOD_c$). By means of the concept of the equivalent elastic crack, the parameters, K_{Ic} and $CTOD_c$, can be calculated using geometric functions based on the LEFM solution:

$$K_{Ic} = \sigma_{Nu} \sqrt{\pi a_{ec}} k_1(\alpha_{ec}) \tag{2.26}$$

and

$$CTOD_c = CMOD_{ec}\, k_2(\frac{a_{ec}}{D}, \frac{a_0}{a_{ec}}) \ , \tag{2.27}$$

where

$$CMOD_{ec} = \frac{4\sigma_{Nu} a_{ec}}{E} k_3(\alpha_{ec}) \ . \tag{2.28}$$

In order to determine the effective elastic crack length in (2.26) and (2.27), the effective elastic crack compliance is assumed to be equal to the unloading compliance in Figure 2.5. Applying this assumption to (2.27) leads to, one obtains

$$E = \frac{4c_N a_0}{C_i Dt} k_3(\alpha_0) \quad \text{and} \quad E = \frac{4c_N a_{ec}}{C_u Dt} k_3(\alpha_{ec}) \ . \tag{2.29}$$

where c_N is a nondimensional constant proportional to the nominal strength. The calculation of a_{ec} results in the determination of the two fracture parameters, K_{Ic} and $CTOD_c$, which provide the nominal strength.

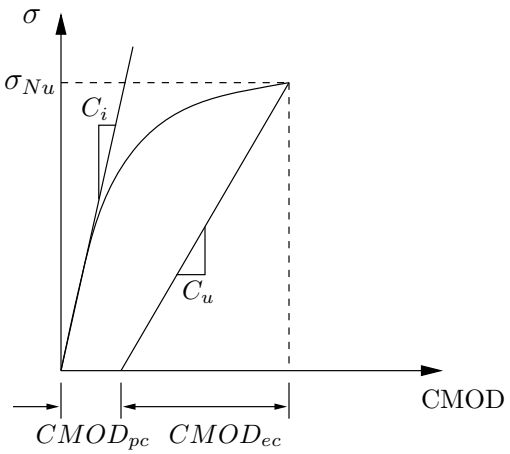

Figure 2.5: Loading-unloading procedure in the TPFM

2.4.3 Relationship between the SEM and the TPFM

Though both the SEM and the TPFM include the equivalent elastic crack concept, the fracture parameters they calculate from the experiment are different. While the SEM determines

G_f and c_f, the TPFM calculates K_{Ic} and $CTOD_c$. We will now illustrate the relationship between the fracture parameters of the SEM and those of the TPFM. Next, the size effect in the TPFM will be discussed [6].

In order to connect the relationship between c_f and $CTOD_c$, we will consider a far field critically stressed ($\sigma_{\infty u}$) infinite plate with a central crack of length $2a_0$. This is because the critical effective crack extension, c_f, is generally regarded as a material property for the infinite structure size. First, we will solve for a_{ec} by using K_{Ic} (2.30) and $CTOD_c$ (2.32) expressions, which is equivalent to c_f for the infinite structure size. The stress intensity factor for the infinite plate is given by

$$K_{Ic} = \sigma_{\infty u}\sqrt{\pi a_{ec}} \ . \tag{2.30}$$

The crack opening width (w_c) is obtained by the crack tip displacement field solution,

$$w_c = \frac{4\sigma_{\infty u}}{E}\sqrt{{a_{ec}}^2 - x^2} \ , \tag{2.31}$$

where x is the distance from the center of the crack. To substitute the crack tip coordinate (a_0) into x, we obtain

$$CTOD_c = \frac{4\sigma_{\infty u}}{E}\sqrt{a_{ec}^2 - a_0^2} \ . \tag{2.32}$$

Then, from (2.30) and (2.32), we solve for the nominal strength

$$\sigma_{\infty u} = \frac{K_{Ic}}{\sqrt{\pi a_0}}\left[\sqrt{1 + c/a_0} - c/a_0\right]^{1/2} \ , \tag{2.33}$$

and the effective crack length, which is given by

$$a_{ec} = a_0 + a_0\frac{1 + c/a_0 - \sqrt{1 + (c/a_0)^2}}{\sqrt{1 + (c/a_0)^2} - c/a_0} \ , \tag{2.34}$$

where

$$c = \frac{\pi}{32}\left(\frac{CTOD_c\, E}{K_{Ic}}\right)^2 \quad . \tag{2.35}$$

Due to the infinite structure size, taking the limit of Δa_{ec} as $a_0 \to \infty$, one obtains

$$\lim_{a_0\to\infty} \Delta a_{ec} = c_f = c = \frac{\pi}{32}\left(\frac{CTOD_c\, E}{K_{Ic}}\right)^2 \quad , \tag{2.36}$$

which defines the relationship between the fracture parameter from the SEM and that of the TPFM. This derivation not only bridges the SEM and the TPFM fracture parameters but also determines constants (B and D_0) of the size effect expression (2.40) in the TPFM.

The size effect on nominal strength in the TPFM can also be derived by considering an infinite structure size. According to the equation (2.21), the nominal strength of a structure with an equivalent crack extension, $\Delta\alpha_{ec}$, can be expressed [6] by

$$\sigma_{Nu} = \frac{K_{Ic}}{\sqrt{Dk^2(\alpha_0 + \Delta\alpha_{ec})}} \quad . \tag{2.37}$$

Similarly to the SEM, taking the Taylor series expansion of the geometric function, one obtains

$$k^2(\alpha_0 + \Delta\alpha_{ec}) = k_0^2 + 2k_0k_0{}'\Delta\alpha_{ec} + \cdots \tag{2.38}$$

so that $\Delta\alpha_{ec}$ is taken out of the geometric function. Since $\Delta\alpha_{ec}$ converges to the c_f/D for an infinite structure size D, the power series expansion of $\Delta\alpha_{ec}$ leads to

$$\Delta\alpha_{ec} = \frac{c_f}{D} + \sum_{n=1}^{\infty} b_n \left(\frac{c_f}{D}\right)^{n+1} \quad . \tag{2.39}$$

Substituting (2.38) and (2.39) into (2.37), one obtains the size effect on the nominal strength, i.e.

$$\sigma_{Nu} = Bf_t{}' \left[1 + \frac{D}{D_0} + c_1\frac{c_f}{D} + c_2\left(\frac{c_f}{D}\right)^2 + \cdots\right]^{-1/2} \quad . \tag{2.40}$$

While the structure size approaches infinity, we can cancel out the c_f/D and its higher order terms resulting in the same size effect expression (2.24), where the constants B and D_0 are also the same as the SEM.

Chapter 3

Cohesive Zone Model

The cohesive zone model (CZM) characterizes the non-linear fracture process zone ahead of a crack tip. Through the determination of the cohesive law for concrete, the non-linear fracture process behavior can be simulated by finite element analysis (FEA). In this chapter, the basic concept of the CZM is explained. Next, the determination of a bi-linear softening curve from experimental fracture parameters is discussed. Finally, FEA implementation and verification of the CZM are illustrated.

3.1 Concept of Cohesive Zone Modeling

In general, the intrinsic CZM consists of four stages (Figure 3.1) containing physical assumptions for a numerical simulation. The first stage is characterized by general elastic material behavior without separation (Figure 3.1: Stage I). We assume the material properties of concrete to be homogeneous and linear elastic at this stage. The next stage is the initiation of a crack when a certain criterion is met, for example, critical hoop stress or strain energy density (Figure 3.1: Stage II). In this study, the fracture initiation criterion for a mode I fracture is assumed to be the state of stress that reaches the cohesive strength (e.g. tensile strength of the concrete, f_t'). Stage III concerns the evolution of the failure governed by the non-linear cohesive law or the softening curve, i.e. the relation between the stress ($\boldsymbol{\sigma}$) and the crack opening width (w) across the fracture surface (Figure 3.1: Stage III). Because

the cohesive law defines the characteristics of the fracture process zone, the shape of the softening curve is essential for the CZM. In our numerical simulation, an intrinsic bi-linear softening curve is introduced in order to characterize the concrete fracture process zone. The final stage is complete failure when the crack opening width reaches the final crack opening width (w_f) (Figure 3.1: Stage IV). Stage IV represents the new surfaces that are generated in which the traction is equal to zero (no load bearing capacity).

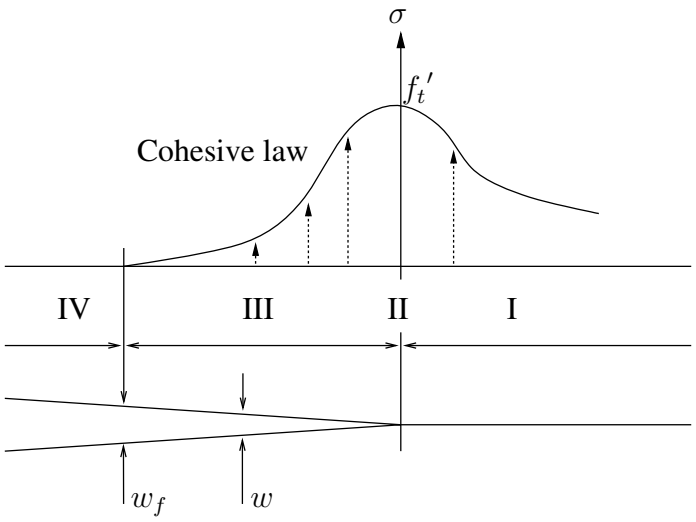

Figure 3.1: Schematic of the cohesive zone model (CZM) concept

3.2 Determination of the Cohesive Law

To characterize the CZM, it is essential to determine the shape of a softening curve. When linear softening was first introduced to the concrete cohesive law [21], the prediction of structural strength was high. Later, Petersson [28] proposed a bi-linear softening curve whose kink point was fixed at ($0.8G_F/f_t'$, $f_t'/3$). Since then, the CZM has utilized bi-linear softening curves without agreement about the precise location of the kink point [6]. Wittmann et al. [37] exploited a bi-linear softening curve with a stress kink point of $0.25f_t'$ for their numerical analysis. Guinea et al. [20] determined a bi-linear softening curve using the tensile strength, the total fracture energy, and two parameters which represent the shape of a

softening curve. Recently, Bazant [9] characterized the bi-linear CZM with three experimental fracture parameters (G_F, G_f and f_t'). In this section, the characteristics of a bi-linear softening curve are discussed along with the features of a bi-linear softening curve. The kink point calculation based on experimental fracture properties is discussed in Chapter 4.

The bi-linear softening curve (Figure 3.2(b)) is adopted in order to define fracture initiation at the cohesive strength, to capture the maximum load of a specimen, and to describe post-peak behavior. The fracture initiation condition, f_t', occurs when the crack opening equals the critical crack opening width (w_{cr})

$$f_t' = f_{cohesive\ law}(w_{cr}) \ . \tag{3.1}$$

The peak load of a specimen is represented by the initial slope of the softening curve which is related to the initial fracture energy measured by the size effect model (SEM) or by the two-parameter fracture model (TPFM). Finally, the post-peak load behavior is characterized by the tail of the softening curve, which is related to the difference between the total fracture energy (G_F) and the initial fracture energy (G_f).

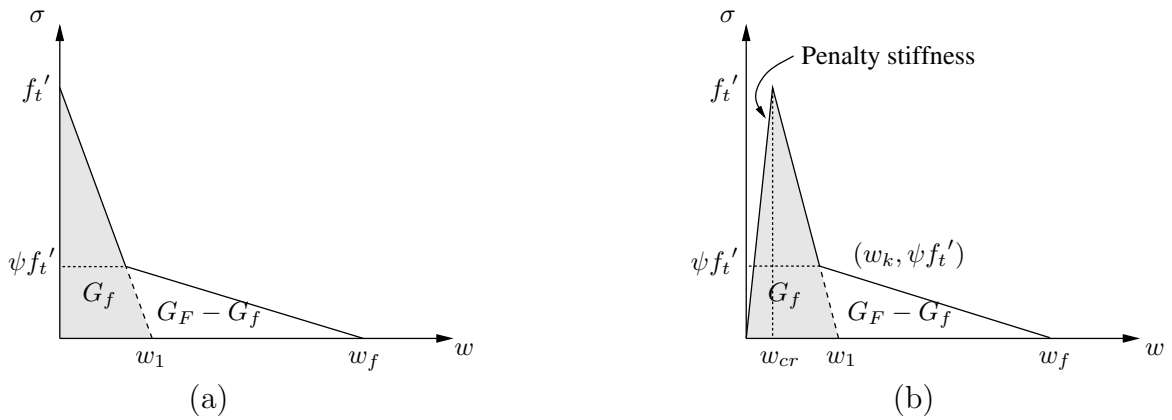

Figure 3.2: The softening curve; (a) extrinsic CZM and (b) intrinsic CZM

In order to determine the coordinates of an intrinsic bi-linear softening curve, we need five unknown constants, f_t', w_{cr}, w_1, w_f and ψ, as shown in Figure 3.2(b). Since initial penalty stiffness is determined based on the numerical stability considerations associated

with a user-defined subroutine (e.g. UEL in ABAQUS), the ratio of f_t'/w_{cr} is fixed, and therefore only four parameters are required. Four unknown constants (f_t', w_1, w_f and ψ) are obtained by the four experimental fracture parameters: the initial fracture energy (G_f), the total fracture energy (G_F), the critical crack tip opening width ($CTOD_c$) and the concrete tensile strength (f_t'). The horizontal axis intercept of the initial descending line is expressed by

$$w_1 = \frac{2G_f}{f_t'} \ , \tag{3.2}$$

because the initial fracture energy is defined as the area under the first and second slope of the curve in Figure 3.2(b). Next, the ratio of the kink point is considered to be

$$\psi = 1 - \frac{CTOD_c \, f_t'}{2G_f} \tag{3.3}$$

which is addressed in Chapter 4. Finally, the horizontal axis intercept of the tail of the softening curve is defined as the final crack opening width

$$w_f = \frac{2}{\psi f_t'} \left[G_F - (1-\psi) G_f \right] \ , \tag{3.4}$$

whose expression is obtained by equating the total fracture energy with the area under the bi-linear softening curve.

3.3 Numerical Implementation and Verification

3.3.1 FEA Implementation

In the numerical simulation, the cohesive surface element is introduced to represent the CZM from elastic behavior (stage I) to complete failure (stage IV). The stress in stage I is a function of strain ($\boldsymbol{\epsilon}$), while the stress in stages III and IV is expressed as a function of the crack opening width. In order to satisfy the different variables of the stress function,

two different elements are used in cohesive zone modeling. One is the general linear elastic element, called the bulk element, which has the stress and strain relationship

$$\boldsymbol{\sigma}_{bulk\ element} = f_{elastic}(\boldsymbol{\epsilon}) \ . \tag{3.5}$$

The bulk element employs two-dimensional plane stress assumptions to represent the linear elastic behavior in stage I. The other element is the cohesive surface element, which has the following traction and separation relationship

$$\boldsymbol{\sigma}_{cohesive\ element} = f_{cohesive\ law}(\mathbf{w}) \ . \tag{3.6}$$

It contains the features of the crack initiation criterion (stage II), the non-linear cohesive law (stage III) and the complete failure condition (stage IV). In summary, inserting the cohesive surface element between bulk elements bridges the linear elastic behavior and the fracture propagation.

Extrinsic and Intrinsic Cohesive Zone Models

There are two ways to insert a cohesive surface element between bulk elements. If the cohesive elements are inserted adaptively during a numerical simulation, we call them "extrinsic" because the insertion time and location are determined by the fracture initiation criterion. When the cohesive element is inserted, additional nodes are required so that the cohesive surface element separates the bulk elements. This also leads to a change of element numbering in the finite element analysis due to creation of new separation surfaces. As a result, the extrinsic model requires change of the mesh information during simulation. On the other hand, when the cohesive elements are inserted before a numerical simulation, we call them "intrinsic" CZM as all the cohesive surface elements are predefined, connecting bulk elements with double nodes. Therefore, it is not necessary for the intrinsic model to modify the mesh information during a numerical simulation.

In this study, the intrinsic CZM (Figure 3.2(a)) is employed, rather than the extrinsic CZM (Figure 3.2(b)), because it is simpler. The fracture initiation criterion is secured by introducing penalty stiffness, which causes additional compliance, but its influence is almost negligible when the cohesive surface element is inserted along the crack path rather than throughout a region or the entire specimen.

Mathematical Formulation

The cohesive element is formulated exploiting the principle of virtual work [14]. The internal work consists of two different components. One is elastic behavior with small deformation represented by the internal work of the virtual strain ($\delta\boldsymbol{\epsilon}$) in the domain ($\Gamma$), and the other is fracture behavior with finite deformation described by the internal work of the virtual crack opening displacement ($\delta\mathbf{w}$) along the crack line (Γ_c). Therefore, the summation of these two internal work components is equal to the external work done by the virtual displacement ($\delta\mathbf{u}$) at the traction boundary (Γ)

$$\int_{\Omega} \delta\boldsymbol{\epsilon}^T \boldsymbol{\sigma} d\Omega + \int_{\Gamma_c} \delta\mathbf{w}^T \mathbf{T} d\Gamma_c = \int_{\Gamma} \delta\mathbf{u}^T \mathbf{P} d\Gamma \ , \tag{3.7}$$

where $\mathbf{T}$ is the traction vector along the cohesive zone, and $\mathbf{P}$ is the external traction vector. The first term in equation (3.7) is the internal virtual work of the bulk element, while the second term in the equation denotes the internal virtual work of the cohesive element. The right hand side of equation (3.7) represents the external virtual work. Exploiting the general linear elastic finite element formulation by using the derivative of the shape function matrix ($\mathbf{B}$) and interpolating the crack opening displacement into the nodal displacement through the shape function matrix ($\mathbf{N}$), we obtain

$$\left[\int_{\Omega} \mathbf{B}^T \mathbf{E} \mathbf{B} d\Omega + \int_{\Gamma_c} \mathbf{N}^T \frac{\partial \mathbf{T}}{\partial \mathbf{w}} \mathbf{N} d\Gamma_c\right] \mathbf{u} = \int_{\Gamma} \mathbf{P} d\Gamma \tag{3.8}$$

where **E** is the material tangential matrix for the bulk element. Consequently, the stiffness matrix and load vector of the cohesive surface element are acquired for the numerical implementation of the CZM.

Finite Element Formulation in ABAQUS

The cohesive surface element is implemented using the ABAQUS user element (UEL) subroutine. The nodal coordinates, displacements, user element properties and other information are available in the UEL subroutine, while the right-hand-side (residual force) vector and the stiffness (Jacobian) matrix have to be defined [1]. The residual force vector is defined by the traction vector along the crack surface,

$$\mathbf{T} = \begin{Bmatrix} T_t \\ T_n \end{Bmatrix} , \tag{3.9}$$

while the stiffness matrix is represented by the Jacobian (tangential) matrix of the cohesive element,

$$\frac{\partial \mathbf{T}}{\partial \mathbf{w}} = \begin{bmatrix} \partial T_t/\partial w_t & \partial T_t/\partial w_n \\ \partial T_n/\partial w_t & \partial T_n/\partial w_n \end{bmatrix} . \tag{3.10}$$

For the determination of the traction vector and the Jacobian matrix of the cohesive element, the bi-linear softening of mode I concrete fracture behavior is exploited. The normal traction component (T_n) is defined by the bi-linear softening relationship

$$T_n = \begin{cases} \left(\frac{f_t{}'}{w_{cr}}\right) w_n & (0 < w_n < w_{cr}) \\ -\frac{f_t{}'}{w_1 - w_{cr}}(w_n - w_1) & (w_{cr} < w_n < w_k) \\ -\frac{\psi f_t{}'}{w_f - w_k}(w_n - w_f) & (w_k < w_n < w_f) \\ 0 & (w_n > w_f) \end{cases} . \tag{3.11}$$

The tangential component of the traction vector (T_t) is assumed to be

$$T_t = \left(\frac{f_t{}'}{w_{cr}}\right) w_t , \tag{3.12}$$

which illustrates only elastic behavior, since we are considering a mode I fracture. Then, each component of the Jacobian matrix is obtained by the derivative of the traction vector with respect to the crack opening width

$$\frac{\partial T_t}{\partial w_t} = \frac{{f_t}'}{w_{cr}} \ , \tag{3.13}$$

$$\frac{\partial T_n}{\partial w_n} = \begin{cases} \frac{{f_t}'}{w_{cr}} & (0 < w_n < w_{cr}) \\ -\frac{{f_t}'}{w_1 - w_{cr}} & (w_{cr} < w_n < w_k) \\ -\frac{\psi {f_t}'}{w_f - w_k} & (w_k < w_n < w_f) \\ 0 & (w_n > w_f) \end{cases} \ , \tag{3.14}$$

and

$$\frac{\partial T_t}{\partial w_n} = \frac{\partial T_n}{\partial w_t} = 0 \ . \tag{3.15}$$

Consequently, we acquire the stiffness matrix and the load vector of the cohesive element for implementation into ABAQUS as a UEL subroutine. The complete UEL code is provided in the Appendix.

3.3.2 Verification of the CZM Model

The pure tension test and the double cantilever beam (DCB) test are implemented to verify the CZM model because they can interpret fracture properties, especially the total fracture energy, in the numerical model. The elastic modulus and four fracture parameters of concrete material are provided in Table 3.1. These four fracture properties result in the determination of the bi-linear softening curve (Figure 3.3) as discussed before. Equation (3.3) leads to the

Table 3.1: Material properties of concrete [31]

Young's modulus (E)	Tensile strength (${f_t}'$)	Initial fracture energy (G_f)	Crack tip opening width ($CTOD_c$)	Total fracture energy (G_F)
32 GPa	4.15 MPa	56.57 N/m	0.0186 mm	164 N/m

kink point of the bi-linear softening, while (3.2) and (3.4) provide the horizontal axis intercept of the initial and the final descending curve in Figure 3.3.

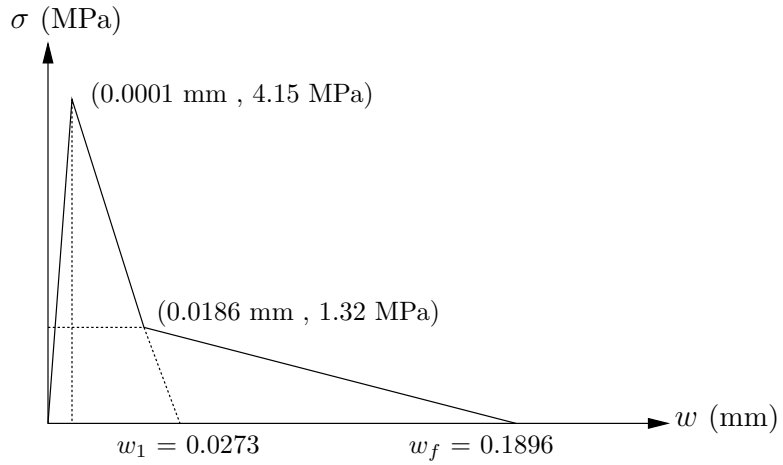

Figure 3.3: Intrinsic bi-linear softening curve based on the fracture properties of concrete (Table 3.1)

Pure tension test

For the pure tension test, a 0.1 by 0.1 plate is elongated at the top under the displacement control. The numerical result of the pure tension test illustrates both the cohesive strength and the total fracture energy of the CZM. The cohesive strength is represented by the peak stress of the plate, while the total fracture energy is an area under the stress (σ) - displacement (δ) curve (164 N/m).

Furthermore, as shown in Figure 3.4, the numerical result of the pure tension test describes the CZM from stage I to stage IV. The linearly increasing line illustrates the linear elastic behavior at stage I with the elastic modulus,

$$E = \frac{\sigma}{\epsilon} = \frac{4.07 \times 10^6}{0.000129} = 31.55 \text{ (GPa)} , \tag{3.16}$$

which is almost the same as the defined Young's modulus (32 GPa). The crack initiation criterion at stage II is also satisfied when the stress of the plate approaches 4.15 MPa. The

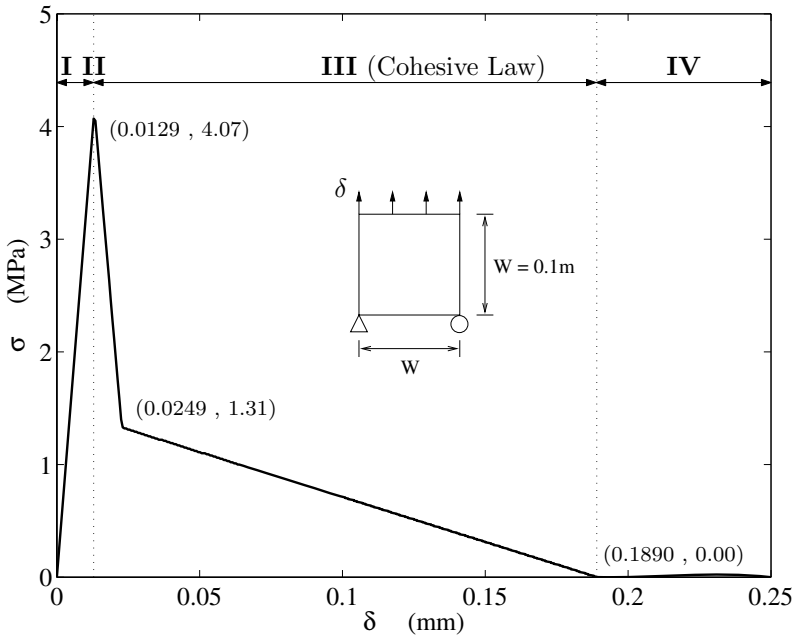

Figure 3.4: Numerical simulation result of pure tension test using CZM model

third part of Figure 3.4 describes the bi-linear cohesive law (Figure 3.3). The stress change point (1.31 MPa) of the numerical result is almost identical to that of the cohesive law in Figure 3.3. Finally, when the top displacement reaches the final crack opening width, the stress of the numerical result is zero, which corresponds with stage IV.

DCB test

The DCB geometry of the simulation is described in Figure 3.5, with the initial notch of the beam ($a_0 = 0.1$m). Figure 3.6 illustrates the mesh of DCB and a view of mesh discretization along the predicted crack path. Through the DCB test, the total fracture energy is verified by comparing the numerical result with the analytical solution.

The DCB problem provides the two analytical solutions for the load (P) - displacement ($\Delta/2$) relationship based on the linear elastic beam theory and the LEFM. The Euler-Bernoulli beam theory provides the relationship between the point load and the displacement

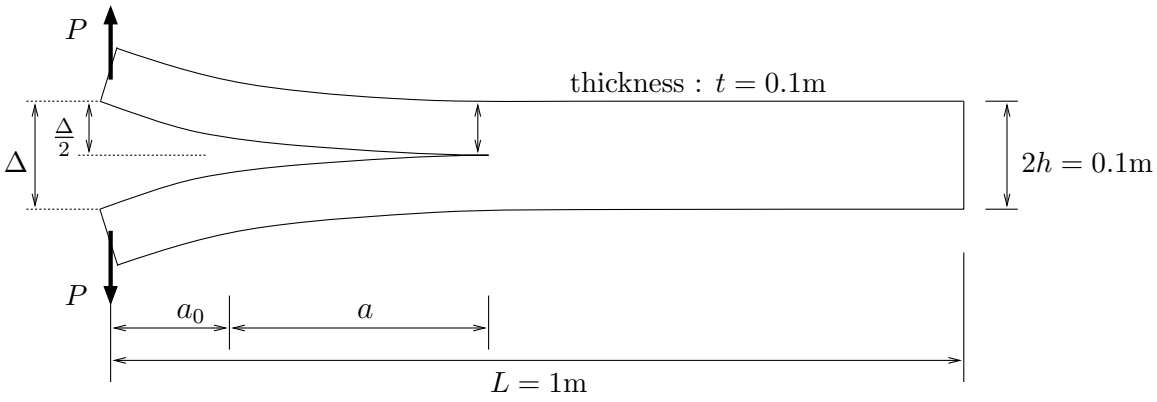

Figure 3.5: Geometry of DCB test

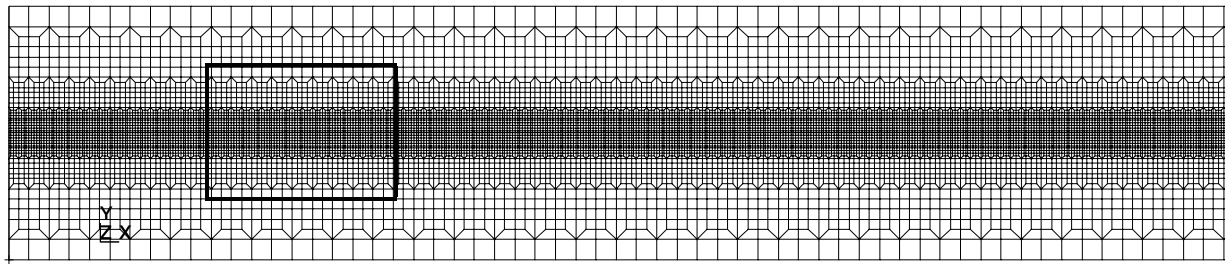

(a)

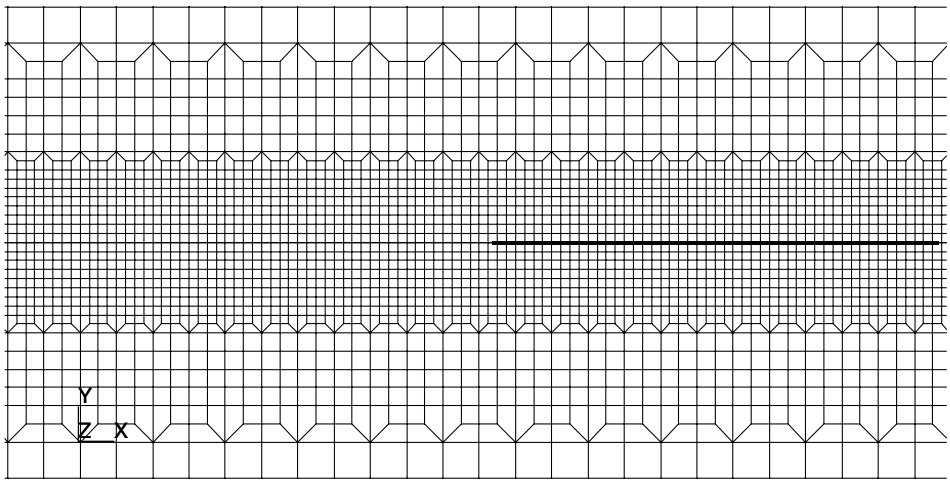

(b)

Figure 3.6: (a) Mesh of DCB problem and (b) zoom of mesh discretization at the cohesive surface element defined.

at the end of the cantilever

$$P = \frac{3EI}{a_0^3}\frac{\Delta}{2} \ . \tag{3.17}$$

The length of the beam is considered to be the initial notch of the DCB (a_0) because no fracture initiation exists in the linear elastic problem. On the other hand, when the crack propagates, the load - displacement relation results from the introduction of the energy release rate, called the total fracture energy, if the LEFM is applicable [2]. The total fracture energy is expressed by

$$G_F = \frac{P^2}{2t}\frac{dC}{da} \ , \tag{3.18}$$

where C is the elastic compliance,

$$C = \frac{\Delta}{P} = \frac{2(a+a_0)^3}{3EI} \ . \tag{3.19}$$

Substituting (3.19) into (3.18) leads to

$$G_F = \frac{12P^2(a+a_0)^2}{t^2h^3E} \ . \tag{3.20}$$

Finally, combining (3.19) and (3.20) results in the load-displacement relationship

$$P = \sqrt[4]{\frac{{G_F}^3 E t^4 h^3}{108}\left(\frac{\Delta}{2}\right)^{-2}} \ . \tag{3.21}$$

When the total fracture energy (G_F), the elastic modulus (E) and the geometry (h, t) of the DCB are defined, (3.21) provides the load-displacement relationship of the DCB based on the LEFM.

Two analytical solutions of the P-$\Delta/2$ relationship are plotted in Figure 3.7 on the basis of the beam theory when beam length is 0.1 (m), and of the LEFM when the total fracture energy is 164 (N/m). The numerical result of the CZM is obtained by the bi-linear softening curve (Figure 3.3) whose total fracture energy is 164 (N/m). The agreement between the

analytical solution of the LEFM and the numerical simulation of the CZM is excellent when $\Delta/2$ is greater than 0.3 mm, as shown in Figure 3.7. The difference between the analytical solution of the beam theory and the numerical simulation of the CZM results from the non-linear fracture process zone in the CZM model. This is because a crack propagates during the numerical simulation of the CZM, whereas no fracture initiation exists in the beam theory.

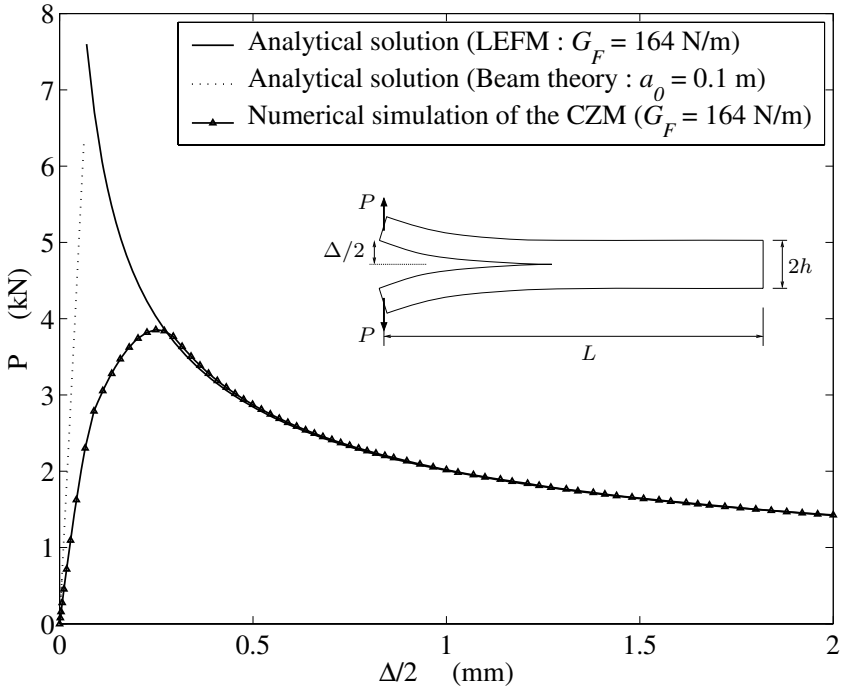

Figure 3.7: Load-displacement relationship of DCB obtained by the analytical solution and by the numerical result

Chapter 4

Determination of the Kink Point in the Bi-linear Softening Model

Although the bi-linear softening curve proposed by Petersson [28] is conventionally employed for the cohesive law of concrete fracture behavior, there is no agreement about the kink point. Petersson assumed the kink point to be fixed at ($0.8G_F/f_t'$, $f_t'/3$), and Wittmann [37] used a stress kink point of $0.25f_t'$. In 2002, Bazant [9] estimated the kink point at the stress change to be between $0.15f_t'$ and $0.33f_t'$. These stress ratios (0.33, 0.25 and 0.15) of the kink point seem not to be based on measured fracture properties but rather on empirical relationships. In this chapter, a method to determine the kink point in the bi-linear softening model is discussed on the basis of experimental fracture parameters (G_f, $CTOD_c$ and f_t'). Then, the proposed method is examined by using experimental fracture parameters and by means of numerical simulations.

4.1 Hypothesis of the Kink Point

In general, although horizontal axis intercepts (x-intercepts) of the first and the second descending slope in a bi-linear softening curve are clearly defined by the concept of the initial fracture energy and the total fracture energy, the stress ratio at kink point (ψ) is usually assumed to be between 0.15 and 0.33 without agreement on the precise location. However, the ratio of the kink point can also be estimated on the basis of four experimental

fracture parameters. This is because only three parameters (f_t', G_f and G_F) are used for the determination of the x-intercepts in a bi-linear softening curve as shown in equations (3.2) and (3.4), though another fracture parameter, c_f or $CTOD_c$, is available. The critical effective crack extension (c_f) is obtained by the SEM, while the critical crack top opening displacement ($CTOD_c$) results from the TPFM. Consequently, the ratio of the stress kink point can be determined by imposing one of two fracture parameters (c_f or $CTOD_c$) into the bi-linear softening curve.

Since the softening curve is a function of the crack opening width, $CTOD_c$ can be explored for the determination of the ratio of the kink point in a bi-linear softening. First of all, $CTOD_c$ is usually between w_{cr} and w_f in the bi-linear softening ($w_{cr} < CTOD_c < w_f$). If $CTOD_c$ is larger than the final crack opening width (w_f), the size of the specimen is large enough for LEFM to be applicable. Next, $CTOD_c$ is generally on the initial slope of the bi-linear softening curve for relatively small specimens because this fracture parameter is considered to be independent of the size. The initial slope of the softening curve also determines the peak load of the specimen [17]. Finally, because $CTOD_c$ and G_f are both calculated when a specimen reaches the peak load, $CTOD_c$ can be large enough to represent the initial fracture energy along the fracture process zone. As a result, it is clear that these three criterion are satisfied when $CTOD_c$ corresponds to the kink point (w_k) of the crack opening width in the bi-linear softening curve. Therefore, the kink point of the crack opening width is assumed as

$$w_k = CTOD_c \ , \tag{4.1}$$

so that $CTOD_c$ relates to size independence and includes the initial fracture energy.

As indicated above, the ratio of the stress at the kink point can be determined by the assumed kink point of the crack opening width. The assumption (4.1) results in the ratio of

the stress kink point for the intrinsic CZM

$$\psi = \frac{w_1 - w_k}{w_1 - w_{cr}} \ . \tag{4.2}$$

Since $w_{cr} \ll w_1$, equation (3.2) and (4.2) lead to

$$\psi = 1 - \frac{CTOD_c \, f_t'}{2G_f} \ , \tag{4.3}$$

which enables us to determine the whole bi-linear softening curve based only on the experimental fracture parameters.

4.2 Experimental Validation

Locations of the kink point calculated by (4.3) are examined by using experimental fracture parameters. For the calculation of the kink point, selected data sets of experimental fracture parameters provide the tensile strength and are obtained either by the TPFM or by the SEM. This is because the location of the kink point is sensitive to f_t', $CTOD_c$ and G_f. Table 4.1 provides data sets of experimental fracture parameters and the ratios of the stress kink points. The shaded boxes are experimental fracture parameters of concrete provided by Roesler et al. [31], Chang et al. [13], and Bazant et al. [10]. White cells in the initial fracture energy column are calculated by the equations (2.1) and (2.29), and white cells in the $CTOD_c$ and in the c_f columns are determined by the equation (2.36). Also, w_1 and ψ are calculated by expressions (3.2) and (4.3), respectively. The ratio of the kink point of the ninth data set is not available, because, in this case, $CTOD_c$ is greater than w_1. However, the range of the calculated ratio is between 0.14 and 0.42, which is in reasonable agreement to the range proposed by Bazant (0.15 - 0.33).

Table 4.1: Fracture parameters of concrete, and the calculation of the ratio of the stress kink point ψ

	Test Age (days)	f_c (MPa)	f_t (MPa)	E (GPa)	w/c	K_{Ic} (MPa m$^{1/2}$)	$CTOD_c$ (mm)	G_f (N/m)	c_f (mm)	w_1 (mm)	ψ
[31]	135	58.3	4.15	32.0	0.42	1.13	0.0180	56.6	25.51	0.0273	0.34
	135	58.3	4.15	32.0	0.42	1.29	0.0202	52.1	24.36	0.0251	0.20
[13]	28	33.9	2.92	22.3	0.3	0.91	0.02076	37.13	25.4	0.0254	0.184
	28	30.1	3.16	19.7	0.3	0.82	0.01355	34.13	10.4	0.0216	0.373
[10]	90	25.2	2.57	33.6	0.65	1.09	0.016	35.36	23.88	0.0275	0.419
	90	27.2	3.14	25.4	0.65	0.732	0.0092	21.10	10.01	0.0134	0.315
	90	39.4	4.29	32.5	0.45	0.958	0.0097	28.24	10.63	0.0132	0.263
		54.8	4.41	37.3	0.25	1.059	0.01	30.07	12.18	0.0136	0.267
[10]	28	26.8	2.58	24.6	0.77	0.992	0.0332	40.00	66.55	0.0310	N/A
	28	39	3.11	33.8	0.64	1.265	0.0263	47.34	48.48	0.0304	0.136
	28	49.4	3.5	34.7	0.5	1.376	0.0261	54.56	42.53	0.0312	0.163
	28	67.5	4.09	37.2	0.36	1.502	0.0242	60.65	35.27	0.0297	0.184
	28	78.2	4.41	40.3	0.2	1.881	0.0262	87.80	30.93	0.0398	0.342

4.3 Numerical Verification

In order to verify the assumption of the kink point, two numerical simulations of the three-point beam-bending test were implemented by using the CZM. One simulation is for a small size beam ($D = 63$ mm), and the other is for a large size beam ($D = 250$ mm). A bi-linear softening curve was determined by four experimental fracture parameters (f_t', G_f, G_F and ψ) from a data set by Roesler et al. [31]. Under the assumption of the kink point given by (4.1), the ratio of the stress kink point (ψ) was 0.34 and the stress at the kink point ($\psi f_t'$) was 1.41 MPa.

Through the numerical simulations, the stress profile along the crack propagation direction was examined at three different points: the pre-peak load (point A), the peak load (point B) and the post-peak load (point C) in the load-CMOD curves (Figure 4.1(a) and 4.2(a)). At the pre-peak load (point A), the stress at the tip of the initial notch (a_0) is higher than the stress at the kink point (1.41 MPa) as shown in Figure 4.1(b) and 4.2(b). When the load reaches the peak point B, the stress at the tip of the initial notch (a_0) nearly corresponds to the stress at the kink point for a small size beam (Figure 4.1(c)) as well as for a large size

beam (Figure 4.2(c)). After the peak load, the stress profile along the crack propagation direction (Figure 4.1(d) and 4.2(d)) demonstrates a large change of slope around the stress kink point, which resembles the bi-linear softening curve. As a result, when the stress at the tip of the initial notch reaches the stress at the kink point, the numerical simulations illustrate that the specimen experiences the maximum load capacity (point B). This is associated with the fact that, experimentally, the initial fracture energy and the critical crack tip opening displacement are calculated at the peak load of the specimens. In other words, the stress profile at the peak load includes the first slope of the bi-linear softening curve.

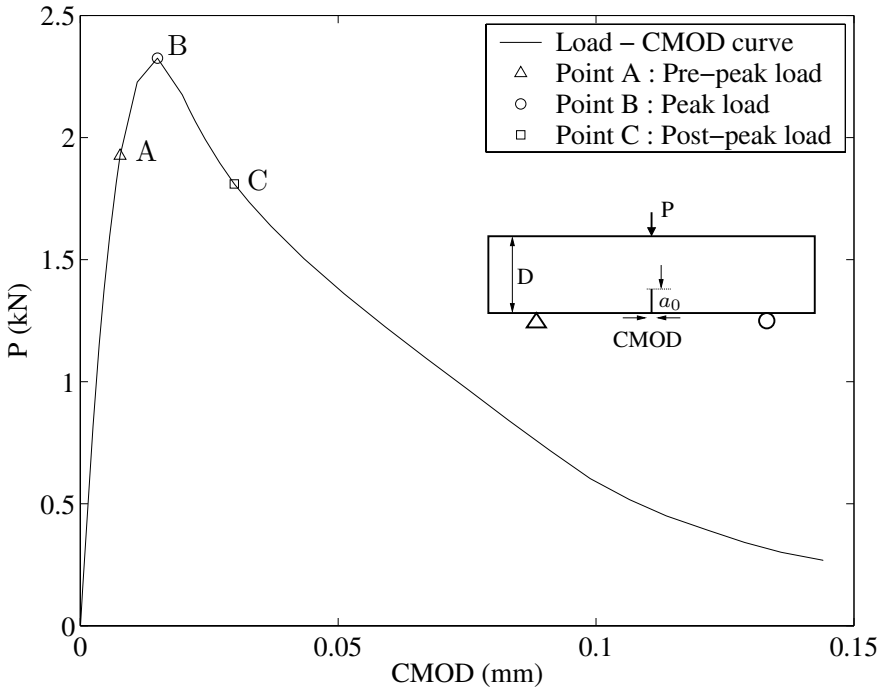
Load – CMOD curve
Point A : Pre–peak load
Point B : Peak load
Point C : Post–peak load
A
B
C
P
D
a_0
CMOD
P (kN)
CMOD (mm)
0
0.5
1
1.5
2
2.5
0.05
0.1
0.15

(a)

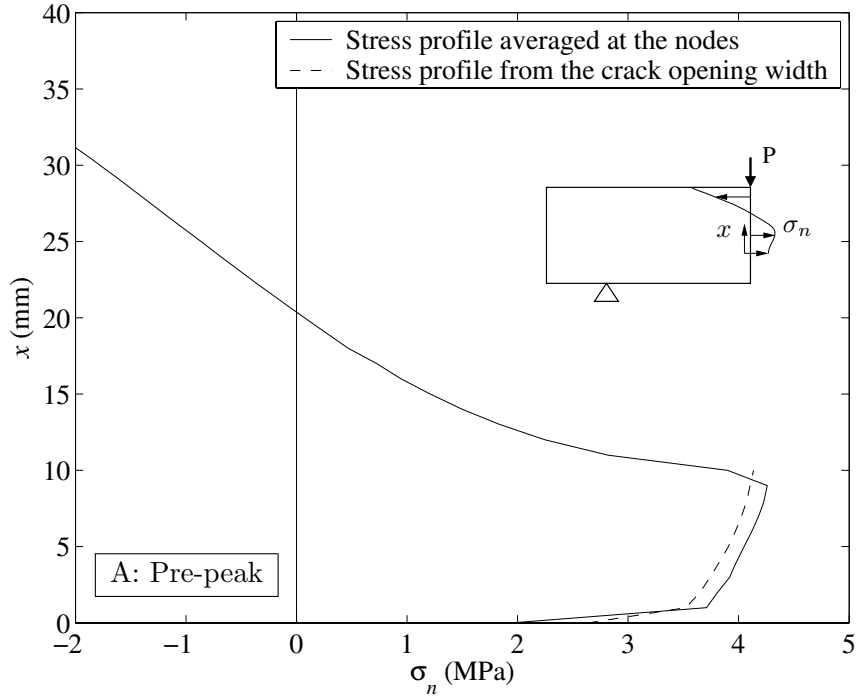
Stress profile averaged at the nodes
Stress profile from the crack opening width
P
x
σ_n
A: Pre-peak
x (mm)
σ_n (MPa)
0
5
10
15
20
25
30
35
40
−2
−1
1
2
3
4
5

(b)

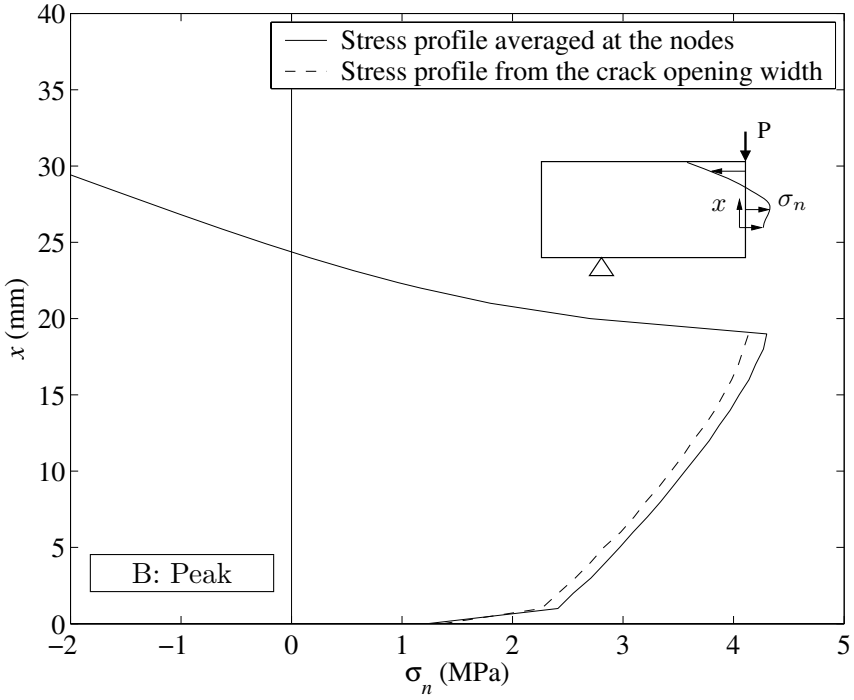

(c)

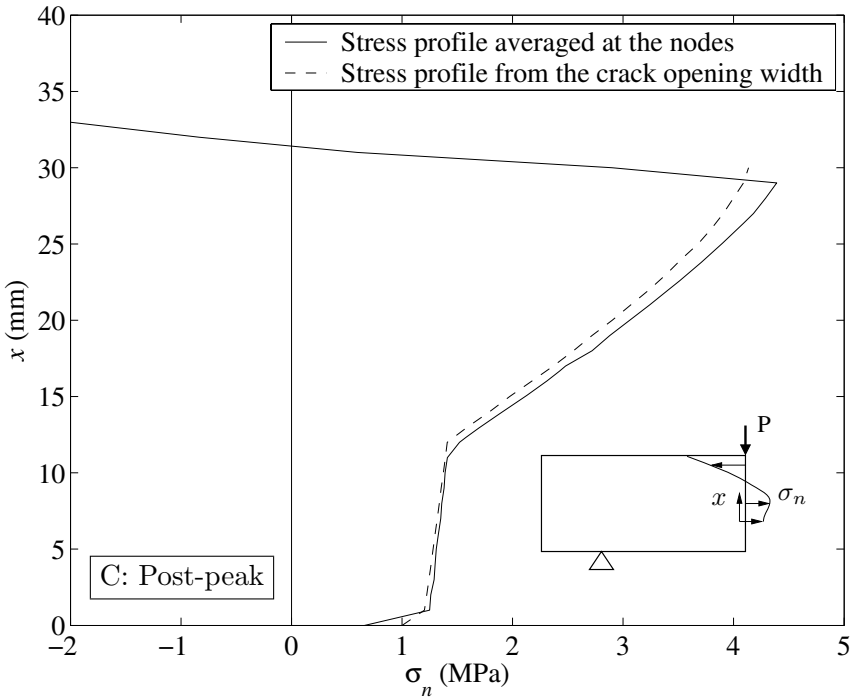

(d)

Figure 4.1: (a) Numerical result of a load-CMOD curve for a small size beam (D = 63mm). (b) Surface normal stress (σ_n) profile along the crack propagation direction at point A, (c) at point B and (d) at point C in the load-CMOD curve.

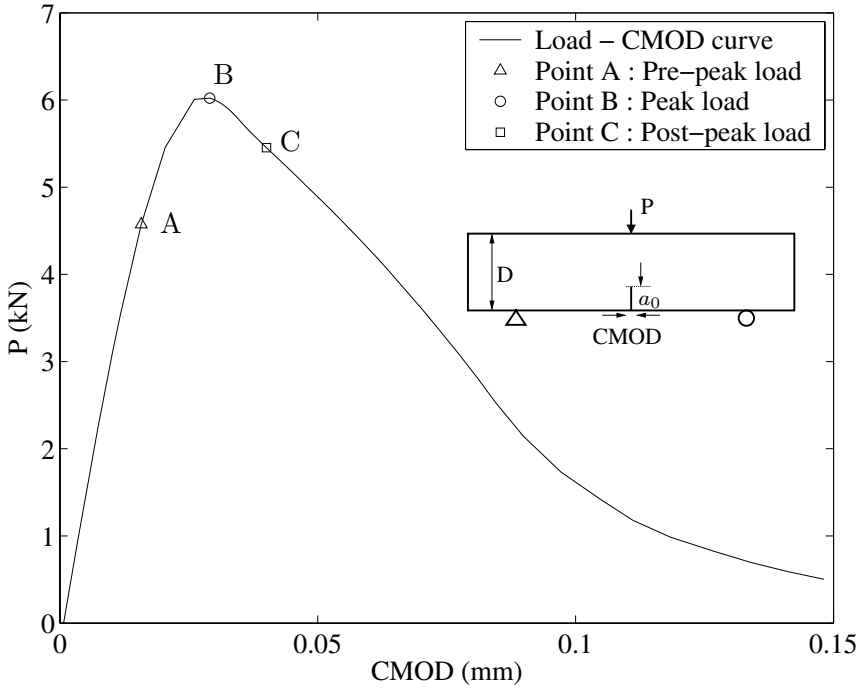
Load − CMOD curve
Point A : Pre−peak load
Point B : Peak load
Point C : Post−peak load
A
B
C
P
D
a_0
CMOD
P (kN)
CMOD (mm)
0
1
2
3
4
5
6
7
0
0.05
0.1
0.15

(a)

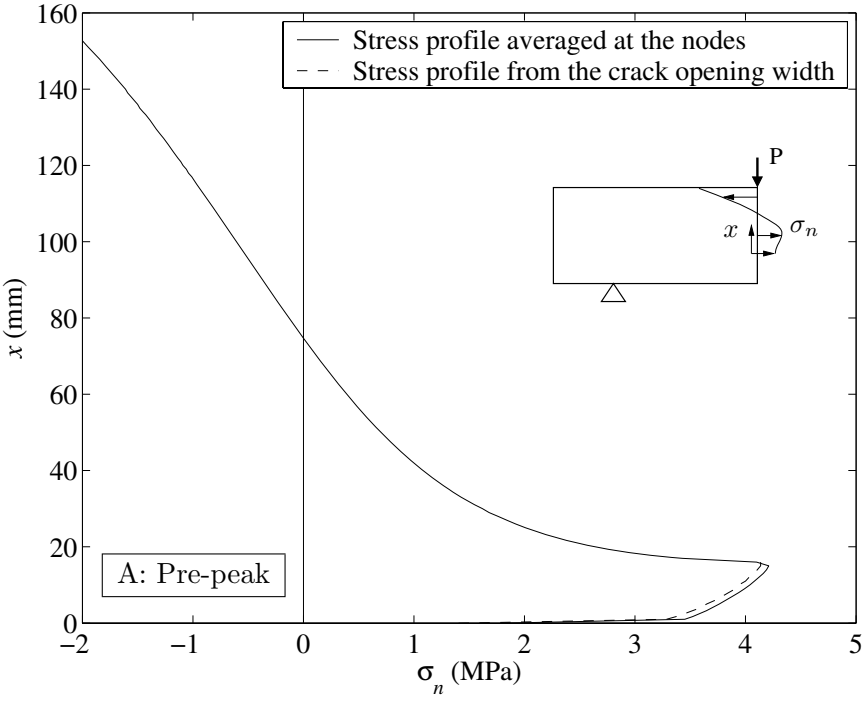
Stress profile averaged at the nodes
Stress profile from the crack opening width
P
x
σ_n
A: Pre-peak
x (mm)
σ_n (MPa)
0
20
40
60
80
100
120
140
160
−2
−1
0
1
2
3
4
5

(b)

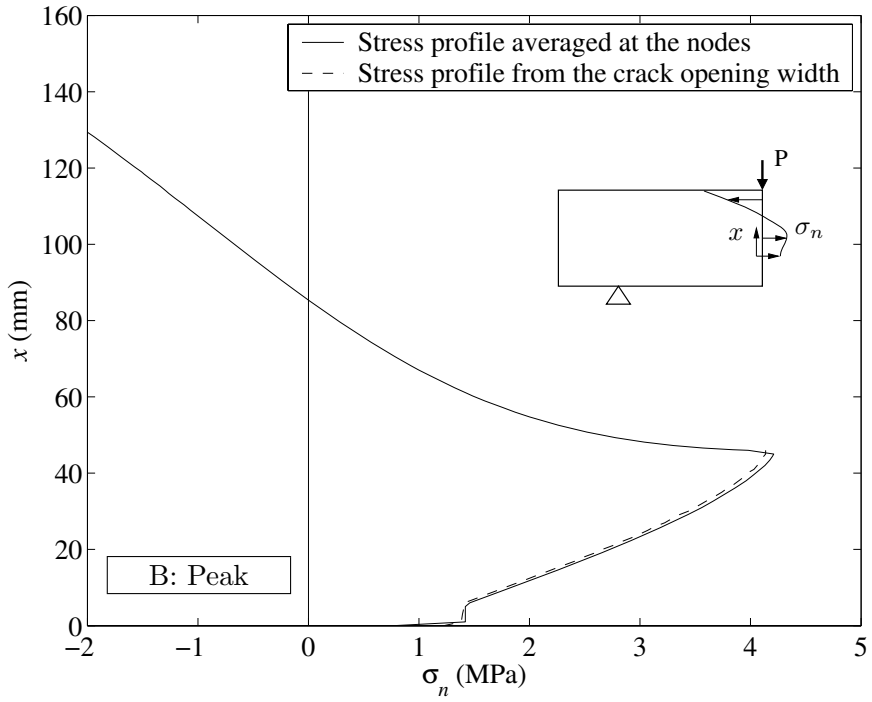

(c)

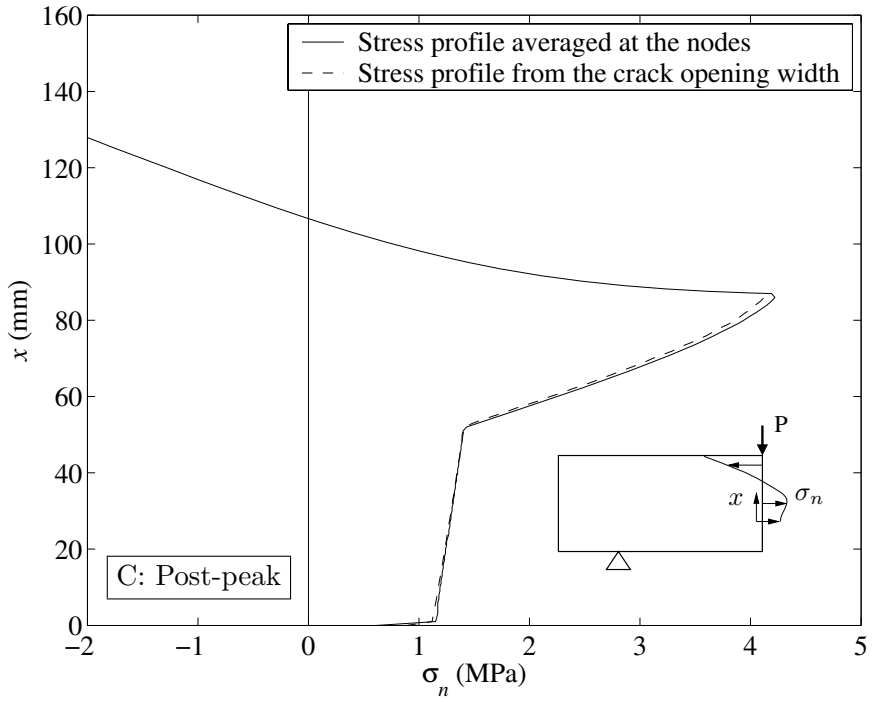

(d)

Figure 4.2: (a) Numerical result of a load-CMOD curve for a large size beam (D = 250mm). (b) Surface normal stress (σ_n) profile along the crack propagation direction at point A, (c) at point B and (d) at point C in the load-CMOD curve.

Chapter 5

Numerical Predictions of the Size Effect in Experiments

Numerical implementations of the CZM not only predict load-CMOD curves but also demonstrate the size effect of geometrically similar notched concrete specimens. In this chapter, experimental geometry and fracture parameters are provided. Then, numerical predictions for load-CMOD curves and for the size effect in the CZM are discussed.

5.1 Experimental Description

In order to determine fracture parameters and to interpret the size effect of concrete, three sizes (D = 63, 150, 250 mm) of notched beams were designed to implement three point bending tests [31]. The geometry and test setup of a three-point bending test are provided in Figure 5.1. The beams represented in Table 5.1 are geometrically similar, with the constant thickness (t = 80 mm), the notch to depth ratio (a_0/D) 1/3, and span to depth ratio (S/D) 4 for each beam size.

Table 5.1: Sizes of the geometrically similar notched beams

Depth (D)	Span (S)	Length (L)	Notch (a_0)	Thickness (t)
63	250	350	21	80
150	600	700	50	80
250	1000	1100	83	80

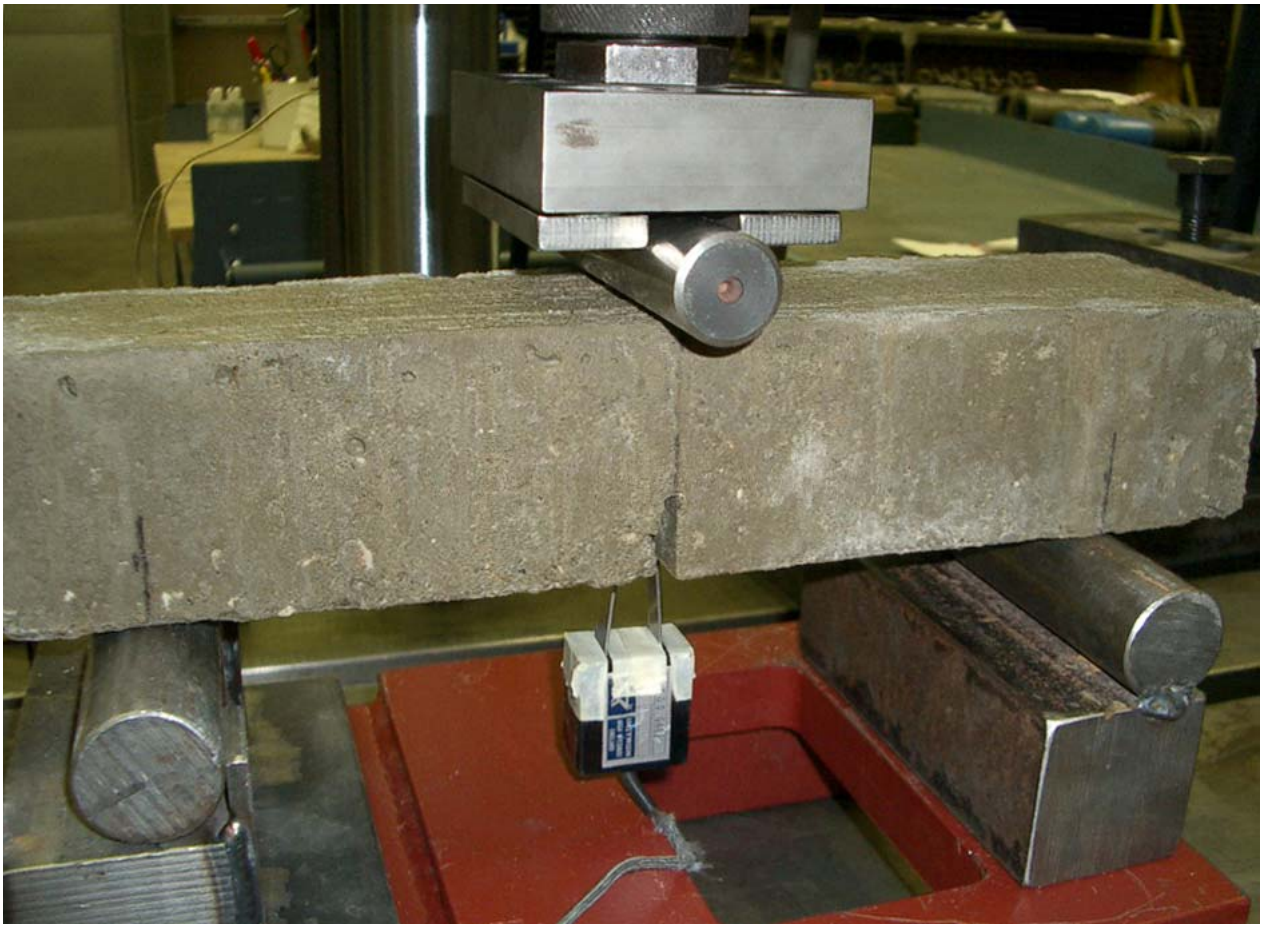

(a)

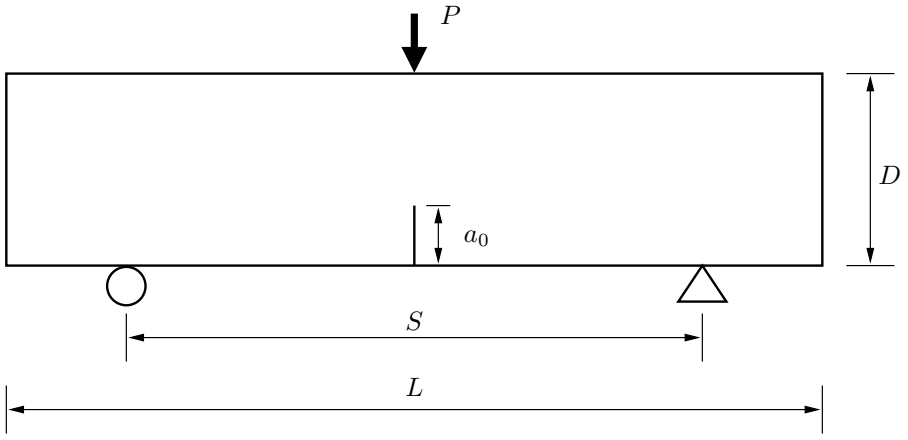

(b)

Figure 5.1: (a) The test setup of a three point bending test; and (b) the specimen geometry.

Three points bending tests of three different sizes provided three fracture parameters (G_F, G_f and $CTOD_c$). The total fracture energy (G_F) were obtained by Hillerborg's work-of-fracture method [22] considering the self-weight of the specimen. The measured total fracture energy increased, as the beam size increased from 63 mm to 150 mm and 250 mm. The other two fracture parameters (G_f, $CTOD_c$) were determined either by the TPFM or by the SEM as discussed in Chapter 2. The TPFM provided the stress intensity factor (K_{Ic}) and the critical crack tip opening width ($CTOD_c$) for each specimen as shown in Table 5.2. Then, the initial fracture energy (G_f) was calculated by the equations (2.1) and (2.29). Because these fracture parameters were considered to be size independent, K_{Ic}, $CTOD_c$ and G_f were averaged for all specimens resulting in 1.13 MPa, 0.0180 mm and 56.6 N/m, respectively. The SEM also enabled us to calculate two fracture parameters: the initial fracture energy (G_f) and the fracture process zone length (c_f), provided in Table 5.2. The critical crack tip opening width ($CTOD_c = 0.0202$ mm) was calculated by the relationship between the SEM and the TPFM (2.36).

Table 5.2: Experimental fracture parameters of concrete obtained by three-point bending tests [31]

Specimen ID	Hillerborg	TPFM		SEM	
	G_F (N/m)	K_{Ic} (MPa-m$^{1/2}$)	$CTOD_c$ (mm)	G_f (N/m)	c_f (mm)
B250 - a	193	1.261	0.0167	52.1	24.36
B250 - b	139	1.203	0.0181		
B250 - c	169	1.497	0.0319		
B150 - a	N/A	N/A	N/A		
B150 - b	170	1.086	0.0255		
B150 - c	159	0.983	0.0115		
B63 - a	N/A	N/A	N/A		
B63 - b	106	1.012	0.0159		
B63 - c	N/A	0.834	0.0115		
CB63 - a	123	1.130	0.0142		
CB63 - b	124	1.002	0.0075		
CB63 - c	123	1.293	0.0184		

In addition to the calculation of these fracture parameters, the modulus of elasticity for the hardened concrete properties was 32.0 GPa, and the split tensile strength was 4.15 MPa which was assumed to be the cohesive strength of concrete.

5.2 Numerical Results of CZM

In numerical simulations, the bilinear rectangular plane stress element (Q4 element) was used for bulk elements, while the cohesive surface elements were inserted between the bulk elements along the known crack path to define the cohesive law. Figure 5.2 illustrates the finite element mesh for specimen size $D = 63$ mm and the cohesive surface elements inserted along the crack path. The size of the cohesive element was selected to be 1 mm so that the element was small enough to represent the cohesive law along the fracture process zone.

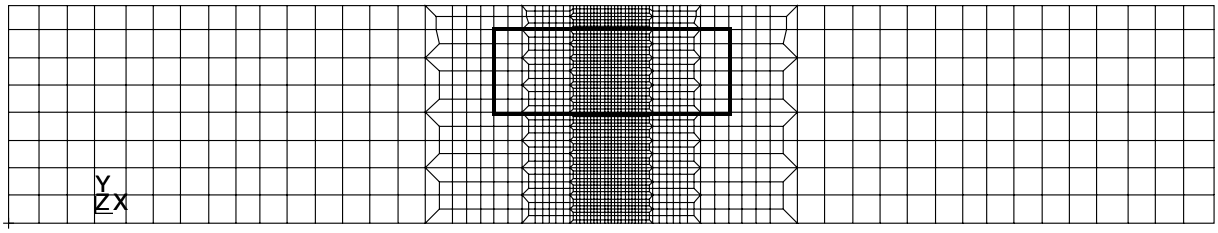

(a)

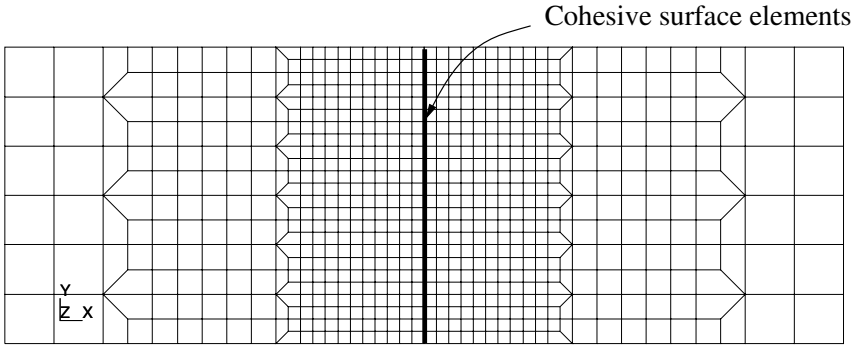

(b)

Figure 5.2: (a) Finite element mesh for specimen size $D = 63$ mm and (b) zoom of mesh along the cohesive element region.

5.2.1 Numerical Prediction

Experimental load-CMOD curves were predicted through numerical simulations of the bi-linear CZM for each specimen size. Fracture parameters are provided in Table 5.3. The determination of the bi-linear softening curve in the CZM was directly based on the fracture properties obtained from the TPFM and the SEM. It is worth mentioning that that it was not necessary for the bi-linear CZM to be calibrated further to force the numerical results to fit with the experimental curves.

The cohesive zone model was run with two separate data sets of fracture parameters, one from the TPFM and the other from the SEM. Table 5.3 provides two data sets of four fracture parameters for each specimen size. The initial fracture energy of the TPFM was 56.6 N/m, while that of the SEM was 52.1 N/m. The stress ratio at the kink point (ψ) was calculated by equating the kink point of the crack opening width (w_k) with the critical crack tip opening width ($CTOD_c$), as discussed in Chapter 4. The TPFM provided a ratio of 0.34 while the SEM yielded a ratio of 0.20. The average tensile strength ($f_t' = 4.15$ MPa) was obtained by the split tensile test. The total fracture energy (average) for each specific specimen size was taken from Table 5.2.

Table 5.3: Fracture parameters in the bi-linear softening curve

Specimen size (D) (mm)	Initial fracture energy (N/m)		Tensile strength (MPa)	Total fracture energy (N/m)	Stress change point (ψ)	
	TPFM	SEM			TPFM	SEM
63	56.6	52.1	4.15	119	0.34	0.20
150	56.6	52.1	4.15	164	0.34	0.20
250	56.6	52.1	4.15	167	0.34	0.20

Figures 5.3 (a), (b) and (c) illustrate the correspondence between the numerical predictions and the experimental results for each specimen size with respect to the normalized load-CMOD curve. For comparison purposes, all the plots are provided on the same scales for the horizontal and vertical axis. There was little difference between two numerical simulation curves from the TPFM and SEM due to the difference of the initial fracture energy

and to the ratio of the stress kink point. The higher initial fracture energy of the TPFM resulted in a slightly larger peak load. Because of the higher ratio of the stress kink point, the post-peak load behavior of the TPFM was higher than that of the SEM after the peak load.

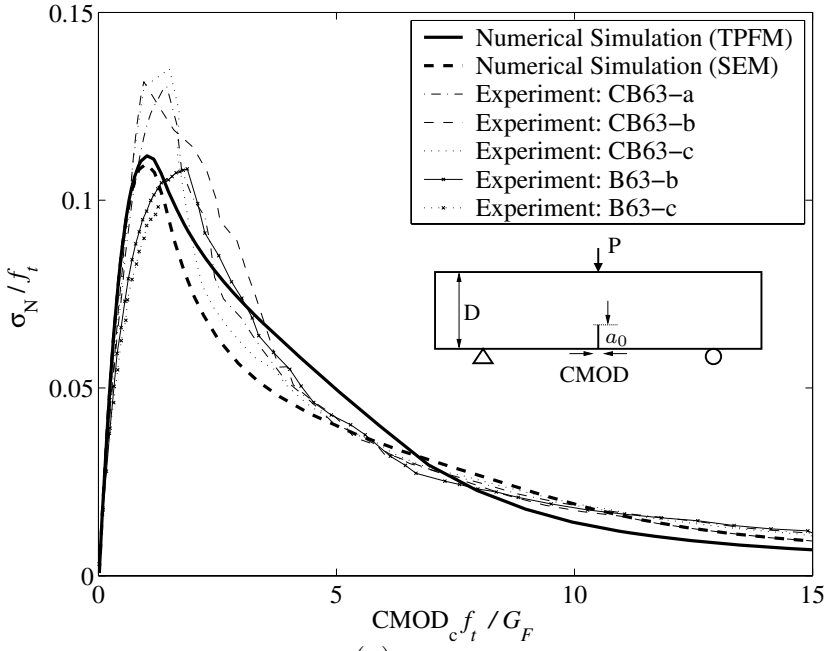

(a)

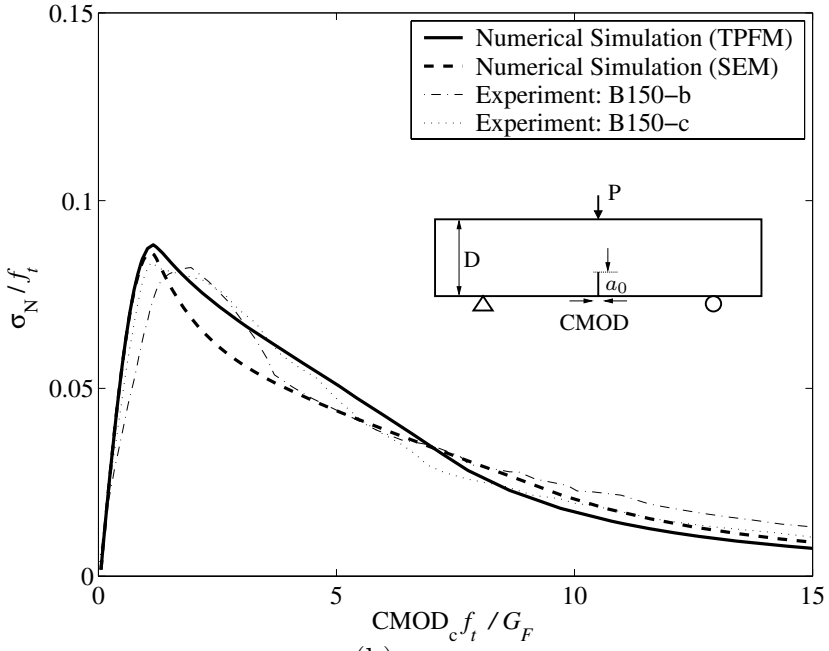

(b)

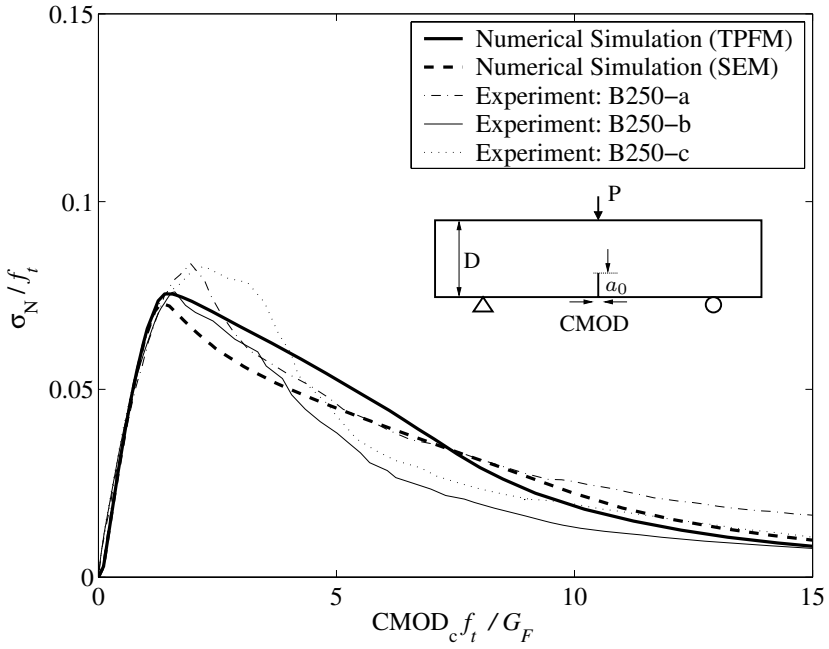

(c)

Figure 5.3: Numerical predictions of load-CMOD curves compared with experimental data: (a) specimen size, D=63mm, (b) specimen size D=150mm, (c) specimen size, D=250mm

The peak load, which is essential for the determination of fracture parameters, was compared to that of the numerical simulation. Although the peak load was under-predicted for the 63 mm and 250 mm beam depth, Table 5.4 shows that the error was less than 10%. In addition to the peak load, the total fracture energy of the experiment was compared to that of the numerical simulation calculated by the load-CMOD curve. The high level of agreement between the experiment and the numerical simulation was obtained, because the experimental total fracture energy was included in the determination of the cohesive law for the numerical simulation.

Table 5.4: Comparison of the peak load and the total fracture energy between experimental data and the numerical simulation

Specimen size (D) (mm)	Peak load (P_c)					Total fracture energy (G_F)				
	Experimental DATA (kN)	Numerical result (kN)		Error (%)		Experimental DATA (kN)	Numerical result		Error (%)	
		TPFM	SEM	TPFM	SEM		TPFM	SEM	TPFM	SEM
63	2.52 (2.05∼2.82)	2.34	2.3	6.99	9.68	119 (106∼124)	115	112	3.5	5.5
150	4.13 (4.09∼4.16)	4.39	4.29	3.98	2.49	164 (159∼170)	156	150	5.9	8.4
250	6.70 (6.31∼6.93)	6.23	6.05	2.73	3.32	167 (139∼193)	165	160	1.0	4.5

5.2.2 Model Sensitivity

The sensitivity of the numerical prediction of the load-CMOD curve for the four experimental fracture parameters (G_f, f_t', G_F and ψ) was investigated. These four fracture parameters in the bi-linear softening curve are listed in Table 5.5. Figures 5.4, 5.5, 5.6 and 5.7 show the results of predicted load-CMOD curves compared with experimental data.

Table 5.5: Fracture parameters in the bi-linear softening curve for the model sensitivity

	Specimen size (D) (mm)	Initial fracture energy (N/m)	Tensile strength (MPa)	Total fracture energy (N/m)	Stress change point (ψ)
Figure 5.4	150	56.6 / 62.3	4.15	164	0.34
Figure 5.5	150	56.6	4.15 / 5.83	164	0.34
Figure 5.6	63	56.6	4.15	119 / 167	0.34
Figure 5.7	150	56.6	4.15	164	0.34 / 0.15

Sensitivity with Respect to Initial Fracture Energy (G_f)

Larger initial fracture energies produced greater peak loads at failure for a given f_t', G_F and ψ, as shown in Figure 5.4. After the peak load, the two softening curves intersected because both total fracture energies were identical in the bi-linear softening.

Sensitivity with Respect to Tensile Strength (f_t')

The numerical prediction of the measured tensile strength (4.15 MPa) was compared with an additional simulation where the tensile strength (5.83 MPa) was assumed to be 10% of the measured compressive strength. Since the tensile strength was assumed to be the fracture initiation criterion, the peak load was greatly affected by changes in the cohesive strength (f_t'), as shown in Figure 5.5. With greater tensile strength materials for a fixed G_f, G_F, and ψ, the slope of the load-CMOD curve becomes steeper, which corresponds to more brittle behavior.

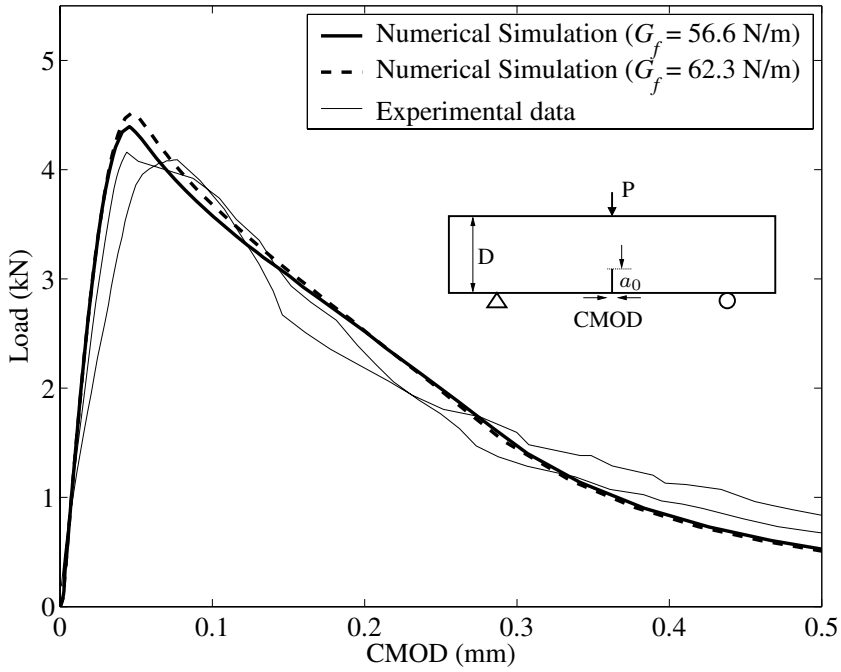

Figure 5.4: Sensitivity of the initial fracture energy to predicted load-CMOD curves (D=150mm).

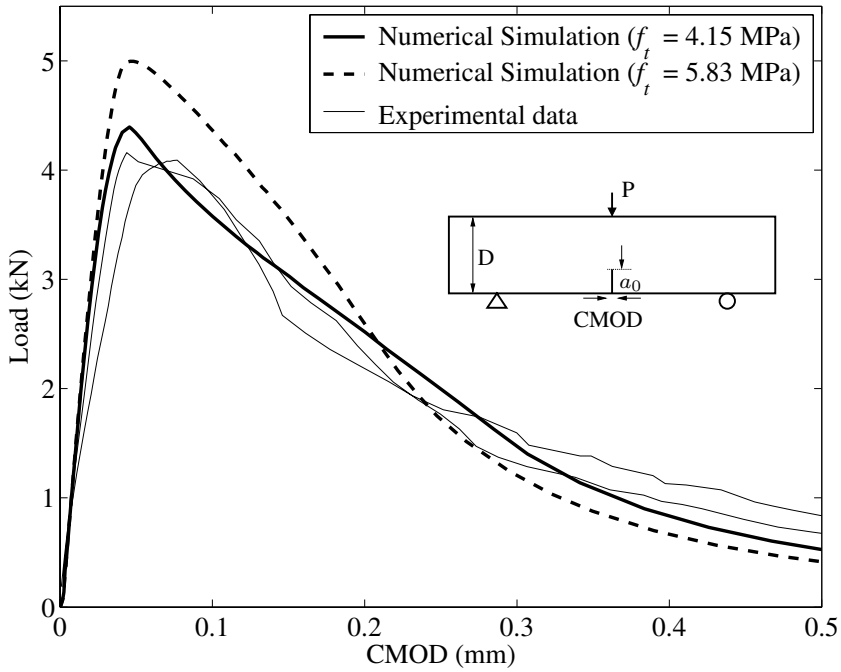

Figure 5.5: Sensitivity of the tensile strength to predicted load-CMOD curves (D=150mm).

Sensitivity with Respect to the Total Fracture Energy (G_F)

The total fracture energy of a 63 mm beam (119 N/m) and that of a 250 mm beam (167 N/m) were compared in order to predict the 63 mm specimen behavior shown in Figure 5.6. As the total fracture energy increased for a fixed G_f, f_t' and ψ, only the post-peak behavior of the specimen was influenced, but not the structure's nominal strength.

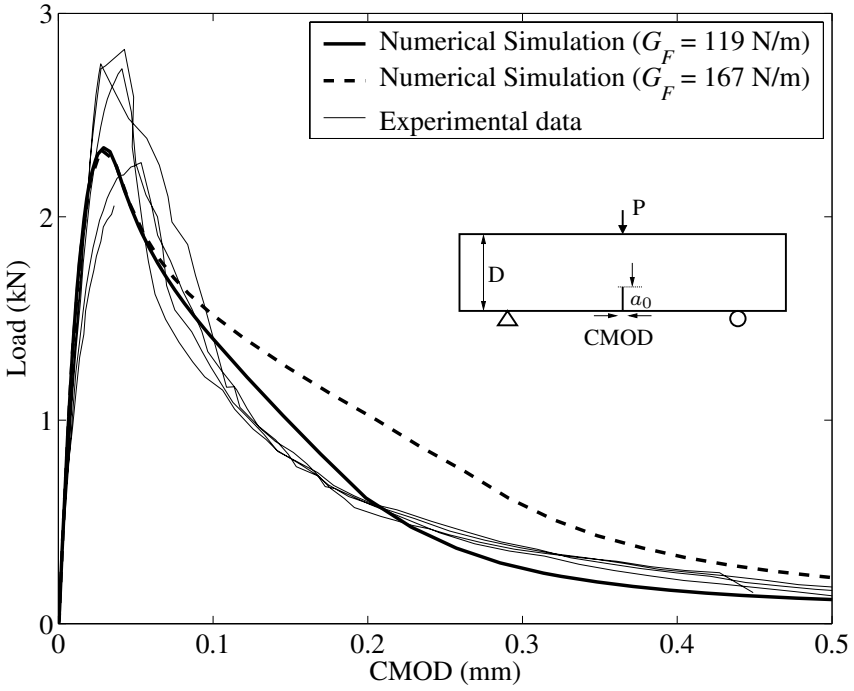

Figure 5.6: Sensitivity of the total fracture energy to predicted load-CMOD curves (D=63mm).

Sensitivity with Respect to the stress ratio of the Kink Point (ψ)

The sensitivity of ψ to the post-peak load behavior was examined through the different ratios of the stress kink point (0.15 and 0.34), as shown in Figure 5.7. The magnitude of the kink point stress does not affect the peak load but as the kink stress ratio increases from 0.15 to 0.34, the tail of the softening curve is extended.

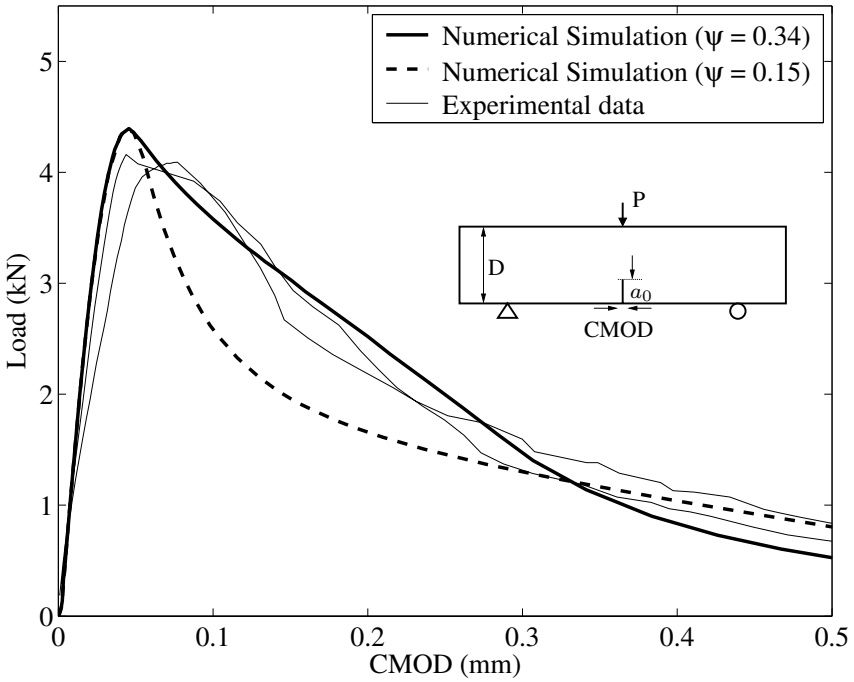

Figure 5.7: Sensitivity of the ratio of the stress at the kink point to predicted load-CMOD curves (D=63mm).

Summary

The initial fracture energy (G_f) and the tensile strength (f_t') are essential parameters to determine the strength of specimens, while the stress ratio of the kink point (ψ) and the total fracture energy (G_F) influence the post-peak behavior as shown in Figure 5.8.

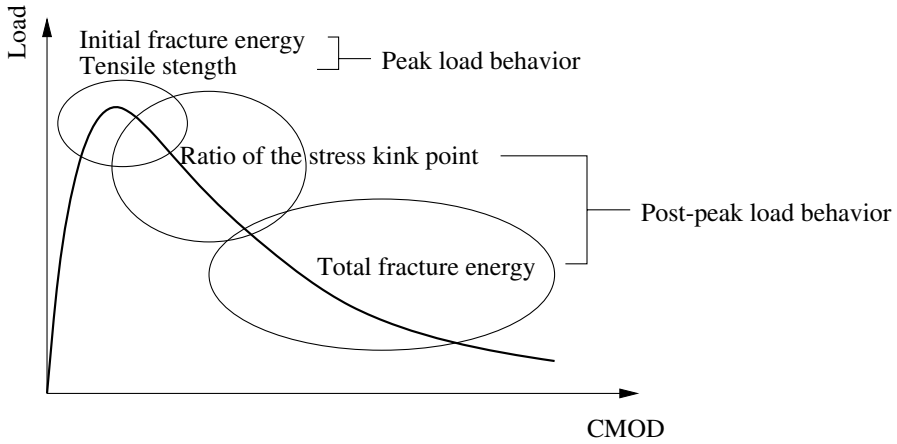

Figure 5.8: Sensitivity of the numerical prediction of a load-CMOD curve for the four fracture parameters (G_f, f_t', G_F and ψ)

5.3 Size Effect in the CZM

The size effect is the change of a structural property, for instance, the nominal strength, the maximum deflection or the maximum strain, while the size of a structure changes. The influence of the structural size (D) on the nominal strength (σ_{Nu}) was examined by the experiment and by numerical simulation. The nominal strength of the experimental and numerical results were assumed to be calculated as the peak load divided by the beam width and thickness. Both experimental and numerical nominal strength are plotted in Figure 5.9 with the size effect equation by Bazant (2.24), which defines the relationship between size and nominal strength. The size effect curve calculated from the SEM parameters closely resembles the curve obtained from the TPFM parameters as seen in Figure 5.9. In conclusion, the nominal strength of both size effect models [4, 26] is similar to that of the experiment and the numerical simulation.

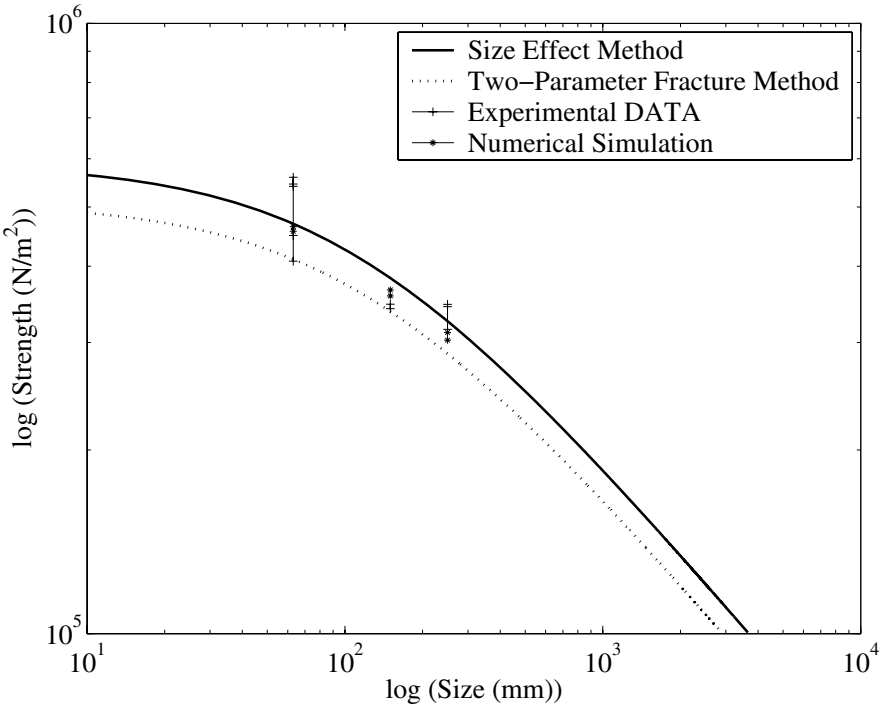

Figure 5.9: Size effect

Chapter 6

Conclusions and Future Studies

This study investigates concrete mode I fracture behavior, with special emphasis on the size effect on the nominal strength of structures. This chapter offers a brief summary and outlines the major contributions of the present work. Then, suggestions for future work to extend this study follow.

6.1 Summary

The size effect is apprehended by two major explanations of non-linear fracture mechanics: the equivalent elastic crack model and the cohesive zone model. The equivalent elastic crack model is the foundation not only of the SEM, proposed by Bazant [4]; but also of the TPFM, proposed by Jenq and Shah [26]. Both the SEM and the TPFM are equivalent for the consideration of the size effect, and provide two size independent fracture parameters.

The cohesive zone model employs the bi-linear softening to characterize the non-linear fracture process behavior of concrete. The determination of the bi-linear softening curve is based directly on four experimental fracture parameters (G_f, f_t', G_F and ψ) without any further calibration or artifact. The initial fracture energy, the tensile strength and the stress ratio at the kink point are the size independent fracture parameters in our model while the total fracture energy depends on specimen size.

The CZM of the bi-linear softening curve for concrete is implemented into a user-defined

subroutine in a commercial finite element software (UEL in ABAQUS) in order to predict load-CMOD curves and to describe the size effect. Initial fracture energy and tensile strength are the essential parameters in the calculation of the peak load of the specimen in the CZM, whereas total fracture energy and the stress ratio at the kink point are sensitive to post-peak load behavior. Moreover, the numerical simulation of the CZM allows representation of the size effect on the nominal strength, which agrees not only with experimental results, but with the size effect equation whose constants are determined by the TPFM and the SEM.

The primary contributions of this study are briefly summarized as follows:

- Experimental load-CMOD curves can be predicted by the bi-linear softening CZM without any artifact or further calibration of the model's fracture parameters.
- The kink point in the bi-linear softening is systematically determined by the experimental fracture parameters ($CTOD_c$, f_t' and G_f) rather than being defined in an ad hoc manner.
- The size effect of the nominal strength for concrete is consistently examined in three different ways: the results of three-point bending tests, the size effect equation proposed by Bazant, and the CZM with bi-linear softening.

6.2 Suggestions for Future Studies

The present study of concrete fracture provides insight for in-depth studies about fiber reinforced concrete, mixed mode problems and other numerical implementation models. Each of those aspects is briefly discussed below.

Fiber Reinforced Concrete

The CZM can also be applicable to fiber reinforced concrete by including a fiber bridging potential in the cohesive law. Furthermore, if the fiber bridge potential is determined by

a fiber volume fraction, a layered concrete with different fiber volume fractions could be simulated by the CZM. For further relevant information on fiber reinforced concrete, the reader is referred to the book by Bentur [11] and Van Mier [34].

Mixed Mode

Although this study of the CZM considers only Mode I fracture behavior, the CZM could be extended to a mixed mode fracture problem. The mixed mode can be represented by introducing effective quantities, for instance, effective opening displacements or effective cohesive tractions [32]. An alternative approach consists of determining separate CZMs corresponding to each independent fracture mode.

Size Effect in the Virtual Internal Bond Model

The virtual internal bond (VIB) model, as proposed by Gao and Klein [18, 27], incorporates the cohesive law into the continuum constitutive law within the framework of hyperelasticity in continuum mechanics. This model could also be exploited for numerical simulations to illustrate the size effect of concrete, especially fiber reinforced concrete. Alternative approaches to the existing ones in the technical literature include modified potential and multi-potentials.

Appendix A

ABAQUS UEL subroutine for CZM

```
c
c ===========================================================================
c   ABAQUS user element (UEL) subroutine
c The UEL is implemented for the two-dimensional cohesive element for mode I.
c The cohesive element has four nodes and two d.o.f. at each node.
c The element numbering is counter-clockwise as shown below.
c       4 +------+ 3
c       1 +------+ 2
c ===========================================================================
    SUBROUTINE UEL (RHS, AMATRX, SVARS, ENERGY, NDOFEL, NRHS, NSVARS,
     & PROPS, NPROPS, COORDS, MCRD, NNODE, U, DU, V, A, JTYPE, TIME,
     & DTIME, KSTEP, KINC, JELEM, PARAMS, NDLOAD, JDLTYP, ADLMAG,
     & PREDEF, NPREDF, LFLAGS, MLVARX, DDLMAG, MDLOAD, PNEWDT, JPROPS,
     & NJPRO, PERIOD)
c
    INCLUDE 'ABA_PARAM.INC'
c
    DIMENSION RHS(MLVARX,*), AMATRX(NDOFEL,NDOFEL), PROPS(*),
     & SVARS(*), ENERGY(8), COORDS(MCRD, NNODE), U(NDOFEL),
     & DU(MLVARX,*), V(NDOFEL), A(NDOFEL), TIME(2), PARAMS(*),
     & JDLTYP(MDLOAD,*), ADLMAG(MDLOAD,*), DDLMAG(MDLOAD,*),
     & PREDEF(2, NPREDF, NNODE), LFLAGS(*), JPROPS(*)
c
    DIMENSION T(mcrd,nrhs),T_d(mcrd,mcrd),w(mcrd),P_l(ndofel,nrhs),
     & P_g(ndofel,nrhs),S_l(ndofel,ndofel),S_g(ndofel,ndofel),
     & R(ndofel,ndofel),R_t(ndofel,ndofel),Shape_N(mcrd,ndofel),
     & Shape_Nt(ndofel,mcrd),coord_l(mcrd,nnode),GP(2),GP_w(2),
     & coords_m(2,mcrd), u1(mcrd), u2(mcrd),
     & store_1(ndofel,mcrd), store_2(ndofel,ndofel)
c ===========================================================================
c Variables to be defined in the UEL subroutine
c   RHS     : Right-Hand-Side vector
c   AMATRX  : Stiffness (Jacobian) matrix
```

```
c Variables available in the UEL subroutine
c   U       : Displacement
c   COORDS  : Original coordinates of the node
c   MCRD    : Largest active degree of freedom (Coordinates parameter)
c   NNODE   : Number of nodes
c Constants from the ABAQUS input for the cohesive zone modeling : PROPS(*)
c   G_f     : Total Fracture Energy
c   G_f1    : Initial fracture energy
c   f_t     : Tensile strength of concrete
c   psi     : Stress at the slop change
c   w_cr    : Critical crack opening width
c   th      : Thickness of the element for 2D
c Variables during calculation
c   T       : Cohesive force law (Softening curve) matrix
c   T_d     : Derivative of the cohesive law matrix
c   w       : Crack opening width vector
c   P_l     : Load vector in local coordinate
c   P_g     : Load vector in global coordinate
c   S_l     : Stiffness matrix in local coordinate
c   S_g     : Stiffness matrix in global coordinate
c   R       : Coordinate transformation matrix
c   coord_l : Deformed configuration in local coordinate system
c   Shape_N : Shape function Matrix
c Constants during calculation
c   w_f     : Final crack opening width
c   w_1     : Intercept of crack opening axis and initial decreasing slop
c   n_GP    : Number of Gauss Point
c   GP      : Gauss points
c   GP_W    : Weight at the Gauss points
c External Functions
c   x1, x2  : Shape functions
c External Subroutines
c   K_COHESIVE_LAW      : Calculate T & T_d
c   K_LOCAL_COORDINATE  : Calculate R & coord_l
c   K_MATRIX_ZERO       : Matrix operation (A = 0)
c   K_MATRIX_TRANSPOSE  : Matrix operation (B = A_t)
c   K_MATRIX_PLUS_SCALAR    : Matrix operation (A = A + c * B)
c   K_MATRIX_MULTIPLY       : Matrix operation (C = A * B)
c ======================================================================
c Input DATA ---------------------------------------------------------
    G_f = props (1)
    G_f1 = props (2)
    f_t = props (3)
    psi = props (4)
    w_cr = props (5)
    th = props(6)
    n_GP = 2
```

```
      data GP   / 0.5773502691896 , -0.5773502691896 /
      data GP_W / 1.0 , 1.0 /
c Initialize ------------------------------------------------------------------
      call k_matrix_zero (rhs,ndofel,nrhs)
      call k_matrix_zero (amatrx,ndofel,ndofel)
      call k_matrix_zero (T,mcrd,nrhs)
      call k_matrix_zero (T_d,mcrd,mcrd)
      call k_matrix_zero (R,ndofel,ndofel)
      call k_matrix_zero (Shape_N,mcrd,ndofel)
c Determine the softening curve -----------------------------------------------
      w_1 = 2*G_f1/f_t
      w_f = 2/(psi*f_t)*(G_f-G_f1+psi*G_f1)
      w_cr = w_cr * w_f
c Change global coordinate into local coordinate ------------------------------
      call k_local_coordinate (R,coords,coord_l,U,ndofel,nnode,mcrd)
      call k_matrix_transpose (R, R_t, ndofel, ndofel)
c Element length : el_length --------------------------------------------------
      do i = 1, mcrd
      coords_m(i,1) = (coord_l(i,1)+coord_l(i,4))*0.5d0
      coords_m(i,2) = (coord_l(i,2)+coord_l(i,3))*0.5d0
      end do
      el_x = coords_m(1,2) - coords_m(1,1)
      el_y = coords_m(2,2) - coords_m(2,1)
      el_length = (el_x**2 + el_y**2)**0.5
c Opeing displacement at the left and right hand side node : u1, u2 ------------
      do i = 1, mcrd
      u1(i) = coord_l(i,4) - coord_l(i,1)
      u2(i) = coord_l(i,3) - coord_l(i,2)
      end do
c Numerical Integration at the Gauss points -----------------------------------
      do i = 1, n_GP
c Crack opening width in tangental and normal direction : w
        do j = 1, mcrd
        w(j) = x1(GP(i))*u1(j) + x2(GP(i))*u2(j)
        end do
c Shape function matrix
        do j = i, mcrd
        Shape_N(j,j) = x1(GP(i))
        Shape_N(j,j+2) = x2(GP(i))
        Shape_N(j,j+4) = -x2(GP(i))
        Shape_N(j,j+6) = -x1(GP(i))
        end do
        call k_matrix_transpose (Shape_N,Shape_Nt,mcrd,ndofel)
c Stiffness matrix & Load vector in local coordinate --------------------------
        call k_Cohesive_Law (T,T_d,f_t,psi,w_1,w_f,w_cr,w,mcrd,nrhs)
        call k_matrix_multiply (Shape_Nt,T_d,store_1,ndofel,mcrd,mcrd)
        call k_matrix_multiply (store_1,Shape_N,S_l,ndofel,mcrd,ndofel)
```

```
        call k_matrix_multiply (Shape_Nt,T,P_l,ndofel,mcrd,nrhs)
c Stiffness matrix & Load vector in global coordinate -------------------------
        call k_matrix_multiply (R_t,S_l,store_2,ndofel,ndofel,ndofel)
        call k_matrix_multiply (store_2,R,S_g,ndofel,ndofel,ndofel)
        call k_matrix_multiply (R_t,P_l,P_g,ndofel,ndofel,nrhs)
c Multiply element length, weight and thickness ------------------------------
        beta = 0.5 * el_length * GP_w(i) *th
        call k_matrix_plus_scalar (amatrx,S_g,beta,ndofel,ndofel)
        call k_matrix_plus_scalar (rhs,P_g,beta,ndofel,nrhs)
        end do
    return
    end
c=======================================================================
c = Shape Functions ====================================================
    function x1(xi)
        INCLUDE 'ABA_PARAM.INC'
        x1 = 0.5*(1 - xi)
    end
    function x2(xi)
        INCLUDE 'ABA_PARAM.INC'
        x2 = 0.5*(1 + xi)
    end
c = Tranction and Jacobian Matrix ======================================
    subroutine K_COHESIVE_LAW (T,T_d,f_t,psi,w_1,w_f,w_cr,w,mcrd,
     &  nrhs)
    INCLUDE 'ABA_PARAM.INC'
    dimension T(mcrd,nrhs), T_d(mcrd,mcrd), w(mcrd)
    w_x = w_1-psi*(w_1-w_cr)
    T(1,1) = f_t/w_cr*w(1)
    T_d(1,1) = f_t/w_cr
    if (w(2) .LE. w_cr) then
        T(2,1) = f_t/w_cr*w(2)
        T_d(2,2) = f_t/w_cr
    elseif ((w(2) .GT. w_cr) .and. (w(2) .LE. w_x)) then
        T(2,1) = (w_1-w(2))*f_t/(w_1-w_cr)
        T_d(2,2) = -f_t/(w_1-w_cr)
    elseif ((w(2) .GT. w_x) .and. (w(2) .LE. w_f)) then
        T(2,1) = (w_f-w(2))*f_t*psi/(w_f-w_x)
        T_d(2,2) = -f_t*psi/(w_f-w_x)
    elseif (w(2) .GT. w_f) then
        call k_matrix_zero (T,mcrd,nrhs)
        call k_matrix_zero (T_d,mcrd,mcrd)
    end if
    return
    end
c = Coordinate translation =============================================
    subroutine K_LOCAL_COORDINATE (R,coords,coord_l,U,ndofel,nnode,
```

```
     & mcrd)
    INCLUDE 'ABA_PARAM.INC'
    dimension R(ndofel,ndofel),coords(mcrd,nnode),coord_l(mcrd,nnode)
     & , U(ndofel)
    dimension co_de(mcrd,nnode), co_de_m(2,2)
c Deformed configuration coordinate ------------------------------------------
    do i = 1, mcrd
    do j = 1, nnode
    co_de(i,j) = coords(i,j) + u(2*(j-1)+i)
    end do
    end do
c Mid point at the deformed configuration ------------------------------------
    do i = 1, 2
    co_de_m(i,1) = (co_de(i,1)+co_de(i,4))*0.5
    co_de_m(i,2) = (co_de(i,2)+co_de(i,3))*0.5
    end do
c Caculate the direction cosine ----------------------------------------------
    d_x = co_de_m(1,2) - co_de_m(1,1)
    d_y = co_de_m(2,2) - co_de_m(2,1)
    d_l = (d_x**2 + d_y**2)**0.5
    cos_a = d_x / d_l
    sin_a = d_y / d_l
c Tanslation(Rotational) Matrix ----------------------------------------------
    do i = 1, nnode
    R(2*i-1,2*i-1) = cos_a
    R(2*i-1,2*i) = sin_a
    R(2*i,2*i-1) = -sin_a
    R(2*i,2*i) = cos_a
    end do
c Change global defomation into local deformation ----------------------------
    do i = 1, nnode
    coord_l(1,i) = R(1,1)*co_de(1,i) + R(1,2)*co_de(2,i)
    coord_l(2,i) = R(2,1)*co_de(1,i) + R(2,2)*co_de(2,i)
    end do
    return
    end
c = Matrix operation ===========================================================
    subroutine K_MATRIX_ZERO (A,n,m)
    INCLUDE 'ABA_PARAM.INC'
        dimension A(n,m)
            do i = 1, n
        do j = 1, m
        A(i,j) = 0.d0
        end do
        end do
    return
    end
```

```
      subroutine K_MATRIX_TRANSPOSE (A,B,n,m)
          INCLUDE 'ABA_PARAM.INC'
          dimension A(n,m), B(m,n)
          call k_Matrix_zero (B,m,n)
          do i = 1, n
          do j = 1, m
          B(j,i) = A(i,j)
          end do
          end do
      return
      end
      subroutine K_MATRIX_PLUS_SCALAR (A,B,c,n,m)
          INCLUDE 'ABA_PARAM.INC'
          dimension A(n,m), B(n,m)
          do i = 1, n
          do j = 1, m
          A(i,j) = A(i,j) + c*B(i,j)
          end do
          end do
      return
      end
      subroutine K_MATRIX_MULTIPLY (A,B,C,l,n,m)
          INCLUDE 'ABA_PARAM.INC'
          dimension A(l,n), B(n,m), C(l,m)
          call k_Matrix_zero (C,l,m)
          do i = 1, l
          do j = 1, m
          do k = 1, n
          C(i,j) = C(i,j) + A(i,k) * B (k,j)
          end do
          end do
          end do
      return
      end
c =====================================================================
```

References

[1] ABAQUS, 2002. Version 6.2, Hibbitt, Karlsson & Sorensen Inc., Pawtucket, RI.

[2] Anderson, T.L. 1995. *Fracture Mechanics: Fundamentals and Applications*, CRC Press, Boca Raton.

[3] Barenblatt, G.I. 1959. The formation of equilibrium cracks during brittle fracture: general ideas and hypotheses, axially symmetric cracks, *Applied Mathematics and Mechanics*, **23**, 622-636.

[4] Bazant, Z.P. and Kazemi, M.T. 1990. Determination of fracture energy, process zone length and brittleness number from size effect, with application to rock and concrete, *International Journal of Fracture*, **44**, 111-131.

[5] Bazant, Z.P. 1993. Scaling law in mechanics of failure, *Journal of Engineering Mechanics*, **119**(9), 1828-1844.

[6] Bazant, Z.P. and Planas J. 1998. *Fracture and Size Effect in Concrete and other Quasibrittle Materials*, CRC Press, Boca Raton.

[7] Bazant, Z.P. 1999. Size effect on structural strength: a review, *Archive of Applied Mechanics*, **69**, 703-725.

[8] Bazant, Z.P. 2000. Size effect, *International Journal of Solids and Structures*, **37**, 69-80.

[9] Bazant, Z.P. 2002. Concrete fracture models: testing and practice, *Engineering Fracture Mechanics*, **29**, 165-205.

[10] Bazant, Z.P. and Becq-Giraudon, E. 2002. Statistical prediction of fracture parameters of concrete and implications for choice of testing standard *Cement and Concrete Research*, **32**, 529-556.

[11] Bentur, A. and Mindess, S. 1990, *Fiber Reinforced Cementitious Composites*, Spon Press, London.

[12] Carpinteri, A. 1982. Notch sensitivity in fracture testing of aggregative materials, *Engineering Fracture Mechanics* **16**(4), 467-481.

[13] Chang, T-P. and Shieh, M-M. 1996. Fracture properties of lightweight concrete, *Cement and Concrete Research*, **26**, 181-188.

[14] Cook, R.D., Malkus, D.S. and Plesha, M.E. and Witt, R.J. 2002. *Concepts and Applications of Finite Element Analysis*, John Wiley & Sons, New York.

[15] D'Addetta, G.A. 2004. *Discrete Models for Cohesive Frictional Materials*, Ph.D. Thesis, University Stuttgart.

[16] Dugdale, D.S. 1960. Yielding of steel sheets containing slits, *Journal of the Mechanics and Physics of Solids*, **8**, 100-104.

[17] Elices, E. and Planas, J. 1996. Fracture mechanics parameters of concrete: an overview, *Advanced Cement Based Materials*, **4**, 116-127.

[18] Gao, H. and Klein, P. 1998. Numerical simulation of crack growth in an isotropic solid with randomized internal cohesive bonds, *Journal of the Mechanics and Physics of Solids*, **46**, 187-218.

[19] Griffith, A.A. 1920. The phenomena of rupture and flow in solids, *Philosophical Transactions*, Series A, **221**, 163-241.

[20] Guinea, G.V., Planas, J. and Elices, M. 1994. A general bilinear fit for the softening curve of concrete. *Materials and Structures (RILEM, Paris)*, **27**, 99-105.

[21] Hillerborg, A., Modeer M. and Petersson P.E. 1976. Analysis of crack formation and crack growth in concrete by means of fracture mechanics and finite elements, *Cement and Concrete Research*, **6**, 773-782.

[22] Hillerborg, A. 1985. The theoretical basis of a method to determine the fracture energy G_F of concrete, *Materials and structures (RILEM, Paris)*, **16**, 291-296.

[23] Inglis, C.E. 1913. Stresses in a plate due to the presence of cracks and sharp corners, *Transactions of the Institute of Naval Architects*, **55**, 219-241.

[24] Irwin, G.R. 1957. Analysis of stresses and strains near the end of a crack traversing a plate, *Journal of Applied Mechanics*, **24**, 361-364.

[25] Irwin, G.R. 1961. Plastic zone near a crack and fracture toughness, *Sagamore Research Conference Proceedings*, **4**.

[26] Jenq, Y.S. and Shah, S.P. 1985. Two parameter fracture model for concrete, *Journal of Engineering Mechanics*, **10**, 1227-1241.

[27] Klein, P. and Gao, H. 1998. Crack nucleation and growth as strain localization on a virtual-bond continuum, *Engineering Fracture Mechanics*, **61**, 21-48.

[28] Petersson, P.E. 1981. *Crack Growth and Development of Fracture Zone in Plain Concrete and Similar Materials*, Report No. TVBM-1006, Division of Building Materials, Lund Institute of Technology, Lund, Sweden.

[29] Phillips, R. 2001. *Crystals, Defects and Microstructures: Modeling Across Scales*, Cambridge University Press, New York.

[30] Rice, J.R. 1968. A path independent integral and the approximate analysis of strain concentration by notches and cracks, *Journal of Applied Mechanics*, **35**, 379-386.

[31] Roesler, J., Paulino, G.H., Park, K. and Gaedicke, C. Concrete fracture prediction using bi-linear softening, (*in preparation).*

[32] Ruiz, G., Pandolfi, A. and Ortiz, M. 2001. Three-dimensional cohesive modeling of dynamic mixed-mode fracture, *International Journal for Numerical Methods in Engineering*, **52**, 97-120.

[33] Shah, S.P., Swartz S.E. and Ouyang C. 1995. *Fracture Mechanics of Concrete*, John Wiley & Sons, New York.

[34] Van Mier, J.G.M. 1996. *Fracture Processes of Concrete: Assessment of Material Parameters for Fracture Models*, CRC Press, Boca Raton.

[35] Weibull, W. 1939. The phenomenon of rupture in solids, *Royal Swedish Institute of Engineering Research*, **153**, 1-55.

[36] Williams, E. 1957. Some observations of Leonardo, Galileo, Mariotte and others relative to size effect. *Annals of Science*, **13**, 23-29.

[37] Wittmann F.H., Rokugo K., Bruhwiler E., Mihashi H. and Simopnin P. 1988. Fracture energy and strain softening of concrete as determined by compact tension specimens, *Material Structure (RILEM, Paris)*, **21**, 21-32.